

# Numerical Simulation of Compressible Flows with Immersed Boundaries Using Discontinuous Galerkin Methods

Bachelor thesis by Simone Stange, Department of Computational Engineering

March 31, 2016

Supervisors: Prof. Dr.-Ing. Martin Oberlack, Dr.-Ing. Björn Müller

Department for Fluid Dynamics



TECHNISCHE  
UNIVERSITÄT  
DARMSTADT



---

Simone Katharina Stange  
Matrikelnummer: 2012232  
Studiengang: B. Sc. Computational Engineering

Bachelorarbeit  
Thema: Numerical Simulation of Compressible Flows with Immersed Boundaries Using Discontinuous Galerkin Methods

Eingereicht: March 31, 2016

Betreuer: Dr.-Ing. Björn Müller

Prof. Dr.-Ing. Martin Oberlack  
Fachgebiet für Strömungsdynamik  
Fachbereich Maschinenbau  
Technische Universität Darmstadt  
Otto-Berndt-Str. 2  
64287 Darmstadt

---

# Declaration of Academic Integrity

## **Thesis Statement pursuant to § 22 paragraph 7 of APB TU Darmstadt**

I herewith formally declare that I have written the submitted thesis independently. I did not use any outside support except for the quoted literature and other sources mentioned in the paper. I clearly marked and separately listed all of the literature and all of the other sources which I employed when producing this academic work, either literally or in content. This thesis has not been handed in or published before in the same or similar form.

In the submitted thesis the written copies and the electronic version are identical in content.

## **Erklärung zur Abschlussarbeit gemäß § 22 Abs. 7 APB der TU Darmstadt**

Hiermit versichere ich, Simone Katharina Stange, die vorliegende Bachelor-Thesis ohne Hilfe Dritter und nur mit den angegebenen Quellen und Hilfsmitteln angefertigt zu haben. Alle Stellen, die Quellen entnommen wurden, sind als solche kenntlich gemacht worden. Diese Arbeit hat in gleicher oder ähnlicher Form noch keiner Prüfungsbehörde vorgelegen.

In der abgegebenen Thesis stimmen die schriftliche und elektronische Fassung überein.

Date:

Signature:

---

# Abstract

This thesis deals with the validation and verification of an extension for the fluid simulation software **Bounded Support Spectral Solver (BoSSS)** that has been developed at the chair of fluid dynamics at the Technical University of Darmstadt. This extension, namely **Compressible Navier-Stokes (CNS)** solver, is used for the simulation of compressible flows. It is based on a **Runge-Kutta Discontinuous Galerkin (RKDG)** method, a combination of the **Finite Element Method (FEM)** and the **Finite Volume Method (FVM)**, which is explained in this work.

Furthermore, the simulations described use a mesh that is based on an **Immersed Boundary Method (IBM)**, a method that allows the usage of a very simple rectilinear mesh and a level set which cuts the cells into void and physical region, thus defining a highly parallelisable and easily generated grid.

After the presentation of the **IBM** we verify the **CNS** solver for Euler equations concerning robustness and convergence. The results show that the calculations are robust concerning different cell agglomerations for moderately high orders and have a convergence rate of  $\mathcal{O}(h^{P+1})$ .

The main part of this thesis deals with the evaluation of the **CNS** solver with immersed boundaries for viscous flows using the example of a **2-dimensional (2D)** cylinder for different Reynolds numbers in the laminar steady and the vortex shedding regime. It shows a good accuracy for high-order calculations even on the coarsest meshes.

---

# Contents

<b>Abbreviations</b>	<b>VI</b>
<b>Nomenclature</b>	<b>VII</b>
<b>1. Introduction</b>	<b>1</b>
1.1. Main Goals . . . . .	1
1.2. Outline . . . . .	1
<b>2. Fundamentals</b>	<b>3</b>
2.1. Essential Equations . . . . .	3
2.1.1. Equations of State . . . . .	3
2.1.2. Ideal Gas Law . . . . .	3
2.1.3. Navier-Stokes Equations . . . . .	4
2.2. Dimensionless Measures . . . . .	5
2.2.1. Non-dimensional Ideal Gas Law . . . . .	6
2.2.2. Dimensionless Navier-Stokes Equations . . . . .	6
<b>3. The Runge-Kutta Discontinuous Galerkin Method</b>	<b>7</b>
3.1. DG Space Discretisation . . . . .	7
3.1.1. Discrete Weak Formulation . . . . .	8
3.1.2. Numerical Fluxes . . . . .	8
3.2. RK Time Discretization . . . . .	10
<b>4. The Immersed Boundary Method</b>	<b>13</b>
4.1. The DG Scheme with Immersed Boundaries . . . . .	13
4.2. RK Time Discretisation with Immersed Boundaries . . . . .	14
4.3. Cell Agglomeration . . . . .	15
4.4. Simulation Parameters Concerning Stability and Runtime in BoSSS . . . . .	15
<b>5. Verification of BoSSS for Inviscid Flows</b>	<b>17</b>
5.1. Robustness Study . . . . .	17
5.2. Convergence Study of Mesh Size and Polynomial Degree . . . . .	19
5.3. Conclusion . . . . .	20
<b>6. Evaluation of BoSSS for Viscid Flows</b>	<b>22</b>
6.1. Theory . . . . .	22
6.1.1. The Laminar Steady Regime . . . . .	23
6.1.2. Laminar Vortex Shedding . . . . .	23
6.2. Simulations . . . . .	24
6.2.1. Steady State Simulations ( $Re < 40 - 50$ ) . . . . .	25
6.2.2. Unsteady Simulations ( $Re > 40 - 50$ ) . . . . .	31

---

<b>7. Conclusion</b>	<b>40</b>
<b>8. Bibliography</b>	<b>IX</b>
<b>List of Figures</b>	<b>XII</b>
<b>List of Tables</b>	<b>XIII</b>
<b>A. Appendix</b>	<b>XIV</b>
A.1. Mesh properties . . . . .	XIV

---

# Abbreviations

2D	2-dimensional
3D	3-dimensional
BoSSS	Bounded Support Spectral Solver
CFL	Courant-Friedrichs-Lewy
CNS	Compressible Navier-Stokes
DG	Discontinuous Galerkin
DG( $\cdot$ )CpD( $\cdot$ )	Degree ( $\cdot$ ), Cells per Direction ( $\cdot$ )
DoF	Degrees of Freedom
FEM	Finite Element Method
FVM	Finite Volume Method
IBM	Immersed Boundary Method
ODE	Ordinary Differential Equation
RK	Runge-Kutta
RKDG	Runge-Kutta Discontinuous Galerkin
SIPG	Symmetric Interior Penalty Method

---

# Nomenclature

Notation	Description
$\mathcal{A}$	Physical region of calculation area
$(\cdot)^*$	Dimensionless quantities
$(\cdot)_\infty$	Reference quantities
$a$	Speed of sound
$\mathcal{B}$	Void region of calculation area
$\mathbf{B}$	Source term
$c$	Concentration
$C_D$	Drag coefficient
$C_L$	Lift coefficient
$c_p$	Specific heat capacity at constant pressure
$c_v$	Specific heat capacity at constant volume
$d$	Drag force
$e$	Specific inner energy
$\mathbf{F}_i^c$	Convective flux
$\text{Fr}$	Froude number
$\mathbf{F}_i^\nu$	Viscous flux
$\gamma$	Heat capacity ratio
$\bar{h}$	Specific enthalpy
$\mathcal{I}$	Immersed boundary
$\mathcal{K}$	Cell domain
$l$	Lift force
$\mu$	Dynamic viscosity
$\Omega$	Problem domain
$\Omega_h$	Discretised problem domain
$P$	Polynomial degree
$p$	Pressure
$\varphi$	Level set function
$\Phi$	Cell-local test function
$\text{Pr}$	Prandtl number
$q_i$	Heat flux
$r$	Radius
$\text{Re}$	Reynolds number
$\rho$	Density



Notation	Description
$\rho E$	Inner energy
$s$	Specific entropy
$St$	Strouhal number
$T$	Temperature
$t$	Time
$\tau_{ij}$	Viscous stress tensor
$W^*$	Wake separation length
$\mathbf{x}$	Spatial coordinate vector, $\mathbf{x} = (x, y)^T \in \Omega$

---

# 1 Introduction

The chair of fluid dynamics of the Technical University Darmstadt mainly deals with research in fluid mechanical problems, e.g. multiphase flows, turbulence or thermodynamics. In recent years, they have been developing a **Bounded Support Spectral Solver**, that we will use in this thesis for the simulation of compressible flows with immersed boundaries. **BoSSS** is based on a **RKDG** method that allows distinct grid types and dimensions (**2D**, **3-dimensional (3D)**) and arbitrarily defined polynomial order without losing the ability of being highly parallelisable.

---

## 1.1 Main Goals

This thesis aims at validating the **CNS** solver for both inviscid and viscous compressible flows using a grid defined through immersed boundaries. For inviscid flows, it has already been verified thoroughly by MÜLLER [1], though not for the specific example we will be concentrating on. Within this work, we will consider the flow around a cylinder in a **2D** mesh. First, we will use the inviscid flow in order to validate **BoSSS** concerning robustness and convergence, using the entropy as an error criterion.

After having formed a firm basis for the inviscid cylinder flow simulation, we can then consider the same example for viscous flows using different Reynolds numbers (20, 40, 100, 200) and compare the obtained results as has already been done for **BoSSS** by AYERS [2], who instead of an **IBM** used curved elements to define the grid. We will therefore comply with the structure given by AYERS [2].

---

## 1.2 Outline

In order to gain a fundamental background knowledge of the methods that are used during the simulation, we will give some theory in the first part of this work. The second part, we will devote to the simulation and validation followed by a conclusion.

First, we will enumerate the important equations of fluid mechanics and their dimensionless forms in chapter 2. After that, we will explain the **Discontinuous Galerkin (DG)** method using an example taken from MÜLLER [1] and the **Runge-Kutta (RK)** method in chapter 3. The methodological part of the thesis will then be completed with an introduction to the **IBM** in chapter 4.

The second part starts with the verification of **BoSSS** concerning the Euler equations or inviscid flow, respectively, considering the robustness and convergence of the computations in chapter 5. In chapter 6, we will first give some theory about the viscous flow around a cylinder



---

followed by the results and analysis of the main task of this work.

The thesis will then be closed by a short conclusion and outlook for following works.

---

## 2 Fundamentals

---

### 2.1 Essential Equations

---

In the following, we will introduce the essential equations that form the basis of all methods and results discussed in this thesis.

---

#### 2.1.1 Equations of State

---

First, we will enumerate the basic thermodynamic equations of state that describe the relations between the specific inner energy  $e$ , the local temperature  $T$ , the specific enthalpy  $\bar{h}$ , the pressure  $p = p(\rho, e)$ , the density  $\rho$  and the specific entropy  $s$ . Assuming that all material parameters are constant, we receive

$$e = c_v T \quad (2.1)$$

$$\bar{h} = c_p T = e + \frac{p}{\rho} \quad (2.2)$$

with the material parameters  $c_p$  and  $c_v$  as specific heat capacities at constant pressure and volume, respectively. Using these relations, we can define the heat capacity ratio

$$\gamma = \frac{c_p}{c_v} = \frac{\bar{h}}{e}, \quad (2.3)$$

e.g.  $\gamma = 1.4$  for standard air.

Another essential equation is the relation for the specific entropy

$$T ds = de + p d\rho^{-1}. \quad (2.4)$$

---

#### 2.1.2 Ideal Gas Law

---

The equations of state mentioned above are not yet complete as there is missing a law for the pressure  $p = p(\rho, e)$ . In this thesis, we will limit ourselves to the ideal gas law as we are only

---

modelling standard air ( $\gamma = 1.4$ ).  
The ideal gas law is defined as

$$p = (\gamma - 1)\rho e \quad (2.5)$$

with  $\rho e \in \mathbb{R}^+$  denoting the inner energy.

A definition of the speed of sound is given by

$$a = \sqrt{\left. \frac{\partial p}{\partial \rho} \right|_s}. \quad (2.6)$$

Using this definition combined with the ideal gas law and an equation for the change of entropy, as found in MÜLLER [1], leads to

$$a^2 = \gamma \frac{p}{\rho}. \quad (2.7)$$

For fully isentropic flows, which we will be concentrating on, it also follows that

$$\frac{p}{\rho^\gamma} = \text{const.} \quad (2.8)$$

---

### 2.1.3 Navier-Stokes Equations

---

The **CNS** equations in conservative forms read as

$$\frac{\partial \mathbf{U}}{\partial t} + \frac{\partial \mathbf{F}_i^c(\mathbf{U})}{\partial x_i} - \frac{\partial \mathbf{F}_i^v(\mathbf{U}, \nabla \mathbf{U})}{\partial x_i} = \mathbf{B}, \quad (2.9)$$

with  $\mathbf{U}$  as the conserved flow variables,  $\mathbf{F}_i^c$  and  $\mathbf{F}_i^v$  as the convective and viscous fluxes and  $\mathbf{B}$  as source terms:

$$\mathbf{U} = \begin{pmatrix} \rho \\ \rho v_j \\ \rho E \end{pmatrix}, \quad \mathbf{F}_i^c = \begin{pmatrix} \rho v_i \\ \rho v_i v_j + p \delta_{ij} \\ v_i(\rho E + p) \end{pmatrix}, \quad \mathbf{F}_i^v = \begin{pmatrix} 0 \\ \tau_{ij} \\ \tau_{ij} + q_i \end{pmatrix}, \quad \mathbf{B} = \begin{pmatrix} 0 \\ \rho F_j \\ \rho F_j v_j + Q_i \end{pmatrix}. \quad (2.10)$$

In addition to the denotations in section 2.1.1, we have  $F_j$  as body forces,  $Q_i$  as heat sources, the viscous stress tensor

$$\tau_{ij} = \mu \left[ \left( \frac{\partial v_i}{\partial x_j} + \frac{\partial v_j}{\partial x_i} \right) - \frac{2}{3} \frac{\partial v_k}{\partial x_k} \delta_{ij} \right] \quad (2.11)$$

with the dynamic viscosity  $\mu$  and the heat flux  $q_i$  modelled using Fourier's Law

$$q_i = k \frac{\partial T}{\partial x_i}. \quad (2.12)$$

### Euler Equations

Regarding only compressible inviscid flow, the viscous fluxes and the source terms dissolve ( $\mathbf{F}_i^v = \mathbf{B} = \mathbf{0}$ ) and the Navier-Stokes equations simplify to the so-called Euler equations:

$$\frac{\partial \mathbf{U}}{\partial t} + \frac{\partial \mathbf{F}_x^c(\mathbf{U})}{\partial x} + \frac{\partial \mathbf{F}_y^c(\mathbf{U})}{\partial y} = 0. \quad (2.13)$$

---

## 2.2 Dimensionless Measures

---

For it is much easier to handle dimensionless PDEs, we will introduce some dimensionless measures as found in KRÄMER-EIS [3]. In order to derive these, we need some reference quantities:  $L_\infty$  as a reference length, a reference velocity  $V_\infty$ , reference density  $\rho_\infty$ , reference volume force  $g_\infty$ , reference viscosity  $\mu_\infty$ , reference thermal conductivity coefficient  $k_\infty$  and the gas constant  $R$ . All other reference quantities can be derived from those. In the following, all dimensionless quantities will be marked with an asterisk (\*):

$$\begin{aligned} t^* &= \frac{V_\infty}{L_\infty} \cdot t, & x_i^* &= \frac{1}{L} \cdot x_i, & v_i^* &= \frac{1}{V_\infty} \cdot v_i, & \rho^* &= \frac{1}{\rho_\infty} \cdot \rho, & p^* &= \frac{1}{\rho_\infty V_\infty^2} \cdot p, \\ \mu^* &= \frac{1}{\mu_\infty} \cdot \mu, & k^* &= \frac{1}{k_\infty} \cdot k, & T^* &= \frac{R}{V_\infty^2} \cdot T, & F_j^* &= \frac{1}{g_\infty} \cdot F_j, & \rho E^* &= \frac{1}{\rho_\infty V_\infty^2} \cdot \rho E, \\ Q_i^* &= \frac{L}{V_\infty^3} \cdot Q. \end{aligned} \quad (2.14)$$

In order to derive the non-dimensional form of the CNS equation, we also need the dimensionless operators:

$$\frac{\partial}{\partial t} = \frac{\partial t^*}{\partial t} \frac{\partial}{\partial t^*} = \frac{V_\infty}{L} \frac{\partial}{\partial t^*}, \quad (2.15)$$

$$\frac{\partial}{\partial x_i} = \frac{\partial x_i^*}{\partial x_i} \frac{\partial}{\partial x_i^*} = \frac{1}{L} \frac{\partial}{\partial x_i^*}, \quad (2.16)$$

$$\nabla = \frac{1}{L} \nabla^*. \quad (2.17)$$

---

### 2.2.1 Non-dimensional Ideal Gas Law

---

For a closed system of equations, we have to use the ideal gas law in dimensionless form:

$$p^* = \rho^*(\gamma - 1)e^* \quad (2.18)$$

$$= (\gamma - 1) \left( \rho E^* - \frac{1}{2} \rho^* \mathbf{v}^{*2} \right). \quad (2.19)$$

---

### 2.2.2 Dimensionless Navier-Stokes Equations

---

As we now have all required measures and operators, we can use them to define the dimensionless relations

$$\text{Reynolds Number } \text{Re} = \frac{\rho_\infty V_\infty L}{\mu_\infty} \propto \frac{\text{inertia forces}}{\text{viscous forces}},$$

$$\text{Froude Number } \text{Fr} = \frac{V_\infty}{\sqrt{gL}} \propto \frac{\text{body inertia}}{\text{gravitational forces}},$$

$$\text{Prandtl Number } \text{Pr} = \frac{\mu_\infty c_p}{k_\infty} \propto \frac{\text{viscous diffusion rate}}{\text{thermal diffusion rate}}.$$

Putting all together, we receive the dimensionless Navier-Stokes equations. As they only depend on non-dimensional quantities, we can drop the asterisk:

$$\frac{\partial \mathbf{U}}{\partial t} + \frac{\partial \mathbf{F}_i^c(\mathbf{U})}{\partial x_i} - \frac{\partial \mathbf{F}_i^v(\mathbf{U}, \nabla \mathbf{U})}{\partial x_i} = \mathbf{B} \quad (2.20)$$

with the dimensionless fluxes

$$\mathbf{F}_i^c = \begin{pmatrix} \rho v_i \\ \rho v_i v_j + p \delta_{ij} \\ v_i(\rho E + p) \end{pmatrix}, \quad \mathbf{F}_i^v = \frac{1}{\text{Re}} \begin{pmatrix} 0 \\ \tau_{ij} \\ \tau_{ij} v_j + \frac{\gamma}{\text{Pr}(\gamma - 1)} q_i \end{pmatrix}, \quad \mathbf{B} = \frac{1}{\text{Fr}^2} \begin{pmatrix} 0 \\ \rho F_j \\ \rho F_j v_j \end{pmatrix} + \begin{pmatrix} 0 \\ 0 \\ Q_j \end{pmatrix}. \quad (2.21)$$

---

## 3 The Runge-Kutta Discontinuous Galerkin Method

This thesis deals with the software **BoSSS** that uses a **RKDG** method for the numerical approximation of compressible flows. The **RKDG** method is split into the **DG** method for space discretisation and the **RK** method as an explicit time discretisation. By using an explicit time-marching algorithm, the parallelization is made much easier.

In the following sections we will study the DG and RK methods separately, considering simple examples and using the same notation as in MÜLLER [1].

---

### 3.1 DG Space Discretisation

---

First, we will study the **DG** method which can be seen as combination of the **FVM** and the **FEM**. It aims at combining the advantages of both methods, namely high-order accuracy and hp-adaptivity (**FEM**), as well as conservativity (**FVM**), thus allowing the computation of higher order solutions with adjustable order on each element on a conservative grid. The main concept of the **DG** method is visualised in fig. 3.1.

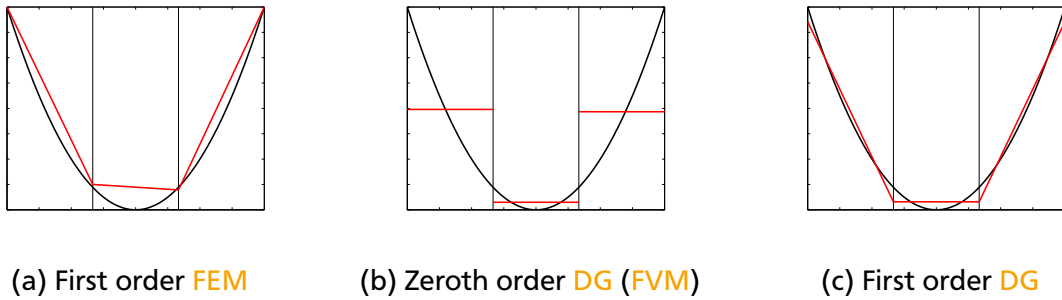


**Figure 3.1.:** Comparison of **FEM**, **FVM** and **DG**

As a simple example that we can use in order to derive the **DG** formulation, we will consider the scalar conservation law

$$\frac{\partial c}{\partial t} + \nabla \cdot f(c) = 0 \quad (3.1)$$

for the concentration  $c = c(\mathbf{x}, t)$  with  $\mathbf{x} \in \Omega \subset \mathbb{R}^D$  and  $t \in \mathbb{R}_0^+$  and a smooth function  $f : \mathbb{R} \rightarrow \mathbb{R}^D$  that also contains suitable initial and boundary conditions.[1]



---

### 3.1.1 Discrete Weak Formulation

---

Our first step of the DG method will be transferring the partial differential equation (3.1) into a weak formulation. Priorly to this, we need a discretisation  $\Omega_h$  of  $\Omega$  consisting of a tessellation of cells  $\{\mathcal{K}_i\}_{i=1,\dots,N}$ , where  $h$  represents a measure for the size of the cells. Each cell  $\mathcal{K}_i$  is of dimension  $D$  with an outward unit normal vector  $\mathbf{n}$ .

After having discretised our geometry, we need a set of cell-local test functions  $\{\Phi_{i,j}\}_{j=1,\dots,M}$  with  $\Phi_{i,j} = \Phi_{i,j}(\mathbf{x}) : \mathbb{R}^D \rightarrow \mathbb{R}$  that forms the basis of the polynomials  $P_{\mathcal{K}_i}(P)$  with maximum degree  $P$ .

In order to obtain the discrete weak formulation, we will now multiply equation (3.1) by  $\Phi_{i,j}$ , integrate over a cell  $\mathcal{K}_i$  and then integrate by parts:

$$\begin{aligned} \frac{\partial c}{\partial t} + \nabla \cdot \mathbf{f}(c) &= 0 \\ \frac{\partial c}{\partial t} \Phi_{i,j} + (\nabla \cdot \mathbf{f}(c)) \Phi_{i,j} &= 0 \\ \int_{\mathcal{K}_i} \frac{\partial c}{\partial t} \Phi_{i,j} dV + \int_{\mathcal{K}_i} (\nabla \cdot \mathbf{f}(c)) \Phi_{i,j} dV &= 0 \\ \int_{\mathcal{K}_i} \frac{\partial c}{\partial t} \Phi_{i,j} dV + \int_{\partial \mathcal{K}_i} (\mathbf{f}(c) \cdot \mathbf{n}) \Phi_{i,j} dA - \int_{\mathcal{K}_i} \mathbf{f}(c) \cdot \nabla \Phi_{i,j} dV &= 0. \end{aligned} \quad (3.2)$$

Considering that the cell's surface  $\partial \mathcal{K}_i$  consists of internal or boundary edges  $\{\mathcal{E}_{i,e}\}_{e=1,\dots,E_i}$  with

$$n(i, e) = \begin{cases} n & \text{if } \mathcal{E}_{i,e} = \mathcal{K}_i \cap \mathcal{K}_n \\ 0 & \text{otherwise} \end{cases} \quad (3.3)$$

where  $n(i, e) = 0$  describes a boundary edge, we can rewrite (3.2) as

$$\int_{\mathcal{K}_i} \frac{\partial c}{\partial t} \Phi_{i,j} dV + \sum_{e=1}^{E_i} \int_{\mathcal{E}_{i,e}} (\mathbf{f}(c) \cdot \mathbf{n}) \Phi_{i,j} dA - \int_{\mathcal{K}_i} \mathbf{f}(c) \cdot \nabla \Phi_{i,j} dV = 0. \quad (3.4)$$

---

### 3.1.2 Numerical Fluxes

---

As the concentration  $c$  is unknown, we need to introduce a modal approximation

$$c(\mathbf{x}, t) |_{\mathcal{K}_i} \approx \bar{c}(\mathbf{x}, t) |_{\mathcal{K}_i} = c_i(\mathbf{x}, t) = \sum_{k=0}^M c_{i,k}(t) \Phi_{i,k}(\mathbf{x}) \quad (3.5)$$

with the Galerkin approach of identical Ansatz and test functions. For we do not enforce continuity on  $\mathcal{E}_{i,e}$ , and thus

$$c_i|_{\mathcal{E}_{i,e}} =: c^- \neq c^+ := c_{n(i,e)}|_{\mathcal{E}_{i,e}}, \quad (3.6)$$

we cannot simply insert the approximation into equation (3.4). Therefore, we will introduce a monotone, Lipschitz continuous numerical flux function @TODO: erklären  $f = f(c^-, c^+, \mathbf{n}) : \mathbb{R}^{D+2} \rightarrow \mathbb{R}$  satisfying the consistency property

$$f(c^-, c^+, \mathbf{n}) = -f(c^+, c^-, -\mathbf{n}). \quad (3.7)$$

By including these definitions into (3.4), we receive

$$\int_{\mathcal{K}_i} \frac{\partial c_i}{\partial t} \Phi_{i,j} dV + \underbrace{\sum_{e=1}^{E_i} \int_{\mathcal{E}_{i,e}} f(c^-, c^+, \mathbf{n}) \Phi_{i,j} dA - \int_{\mathcal{K}_i} \mathbf{f}(c_i) \cdot \nabla \Phi_{i,j} dV}_{=:(\mathbf{f}_i)_j} = 0 \quad (3.8)$$

with the discrete operator  $\mathbf{f}_i = \mathbf{f}_i(t, \mathbf{c}_i) \in \mathbb{R}$ .

Some well-known examples of numerical fluxes contain [4]:

- The Godunov flux
- The Engquist-Osher flux
- The Lax-Friedrichs flux
- The local Lax-Friedrichs flux
- The Roe flux with 'entropy fix',

whereby we will attend to the local Lax-Friedrichs or Rusanov flux, which is defined as

$$f(c^-, c^+, \mathbf{n}) = \frac{\mathbf{f}(c^-) + \mathbf{f}(c^+)}{2} \cdot \mathbf{n} - \frac{C_R}{2} (c^+ - c^-) \quad (3.9)$$

with the coefficient  $C_R$  based on a local stability criterion. In this thesis, we will use an estimate based on the maximum local wave speed that was developed by Toro [5]

$$C_R = \max(|\mathbf{u}^+ \cdot \mathbf{n}| + a^-, |\mathbf{u}^- \cdot \mathbf{n}| + a^+) \quad (3.10)$$

with  $\mathbf{u}^\pm$  and  $a^\pm$  denoting the one-sided normal velocity and the local speed of sound. As the Rusanov flux has a high stability, it will be used disregarding that it is prone to numerical diffusion.

### 3.2 RK Time Discretization

After having studied the spatial discretisation, we will now attend to the time discretisation, using the RK method.

First of all, we need to reformulate equation (3.8) in order to achieve a system of coupled Ordinary Differential Equation (ODE)s.

$$\int_{\mathcal{K}_i} \frac{\partial c_i}{\partial t} \Phi_{i,j} dV + \underbrace{\sum_{e=1}^{E_i} \int_{\mathcal{C}_{i,e}} f(c^-, c^+, \mathbf{n}) \Phi_{i,j} dA - \int_{\mathcal{K}_i} f(c_i) \cdot \nabla \Phi_{i,j} dV}_{=:(\mathbf{f}_i)_j} = 0.$$

The first term of the equation above can be reformulated as

$$\begin{aligned} \int_{\mathcal{K}_i} \frac{\partial c_i}{\partial t} \Phi_{i,j} dV &= \int_{\mathcal{K}_i} \frac{\partial}{\partial t} \left( \sum_{k=0}^M c_{i,k}(t) \Phi_{i,k}(\mathbf{x}) \right) \Phi_{i,j} dV \\ &= \sum_{k=0}^M \frac{\partial c_{i,k}}{\partial t} \underbrace{\int_{\mathcal{K}_i} \Phi_{i,k} \Phi_{i,j} dV}_{=:(\mathbf{M}_i)_{k,j}} \\ &= \mathbf{M}_i \frac{\partial \mathbf{c}_i}{\partial t} \end{aligned}$$

thus leading to

$$\mathbf{M}_i \frac{\partial \mathbf{c}_i}{\partial t} + \mathbf{f}_i = 0 \quad (3.11)$$

with  $\mathbf{M}_i \in \mathbb{R}^{M,M}$  being a cell-local symmetric mass matrix associated with  $\mathcal{K}_i$ . As we have assumed an orthonormal basis  $\{\Phi_{i,j}\}_{j=1,\dots,M}$ , thus reducing the mass matrix to the identity matrix  $I$ , the ODEs simplify to

$$\frac{\partial \mathbf{c}_i}{\partial t} + \mathbf{M}_i^{-1} \mathbf{f}_i = 0 \quad (3.12)$$

$$\frac{\partial \mathbf{c}_i}{\partial t} + \mathbf{f}_i = 0. \quad (3.13)$$

Using an explicit RK method of order  $S$ , we can now advance this system of ODEs and calculate the new coefficients from

$$\mathbf{c}_i(t_1) = \mathbf{c}_i(t_0) - \Delta t \sum_{s=1}^S (\alpha)_s \mathbf{k}_s, \quad (3.14)$$

with a known solution at  $t_0$  to a new instant  $t_1$  and  $\Delta t = t_1 - t_0$ , where

$$\mathbf{k}_s = \mathbf{f}_i \left( t_0 + (\beta)_s \Delta t, \mathbf{c}_i(t_0) + \Delta t \sum_{t=1}^S (\Gamma)_{s,t} \mathbf{k}_t \right). \quad (3.15)$$

The coefficients  $\alpha \in \mathbb{R}^S$ ,  $\beta \in \mathbb{R}^S$  and  $\Gamma \in \mathbb{R}^S$  are specific for each RK method. Those of the most common RK methods are displayed in the Butcher Tableaus (ENRIGHT [6], GOTTLIEB and SHU [7]) in table 3.2. They determine the stability and accuracy of the time integration scheme.

0					
$\beta_2$	$\Gamma_{21}$				
$\beta_3$	$\Gamma_{31}$	$\Gamma_{32}$			
$\vdots$	$\vdots$	$\vdots$	$\ddots$		
$\beta_s$	$\Gamma_{s1}$	$\Gamma_{s2}$	$\cdots$	$\Gamma_{s,s-1}$	
	$\alpha_1$	$\alpha_2$	$\cdots$	$\alpha_{s-1}$	$\alpha_s$

**Table 3.1.:** Butcher Tableau for the Explicit Runge–Kutta Method.

A well-known stability criterion according the explicit Euler time discretisation for linear, hyperbolic PDEs, namely the Courant-Friedrichs-Lewy (CFL) criterion, restrains the temporal step-size  $\Delta t$ :

0   1	0   1   1 1/2   1/2	0   1/3   1/3 2/3   0 1/3 1/4   0 3/4	0   1/2   1/2 1/2   0 1/2 1   0 0 1 1/6   2/6 2/6 2/6
Explicit Euler (first order)	Trapezoidal rule (second order)	Third order TVD (third order)	Classical RK (fourth order)

**Table 3.2.:** Butcher Tableaus for different orders of RK

---



---


$$\Delta t \leq c_{CFL} \frac{h}{\underline{u}} \quad (3.16)$$

with  $\underline{u} \in \mathbb{R}^+$  denoting the largest propagation velocity and a positive constant  $c_{CFL} \leq 1$  depending on the applied spatial discretisation procedure.

Concerning the Euler equations, the largest propagation velocity is given by  $\underline{u} = ||\mathbf{u}|| + a$  and by taking the influence of the approximation order  $P$  into account, we can use the criterion developed by COCKBURN and SHU [8]

$$\Delta t \leq \frac{c_{CFL}}{2P+1} \frac{h}{||\mathbf{u}|| + a} \quad (3.17)$$

as a sufficiently accurate estimate for the stability criterion in this thesis.

---

## 4 The Immersed Boundary Method

In the following chapter, we will study the DG method with immersed boundaries. This chapter is based on MÜLLER, KRÄMER-EIS, KUMMER, *et al.* [9]

IBMs are characteristic in the way of creating the calculation mesh as they do not rely on body fitted grids, but on a level set function  $\varphi$  that cuts the cells into the physical and the void region. It therefore simplifies the mesh generation, as it only needs a cartesian or rectilinear mesh and a function that approximates the level set. Brought along with the cartesian mesh, it is easily parallelisable, thus rendering it convenient for more complex structures that shall be computed on several processors.

---

### 4.1 The DG Scheme with Immersed Boundaries

---

We regard an implicit representation of an immersed boundary using the level set function  $\varphi$  that parts the calculation area  $\Omega_h$  into

- the physical region:  $\mathcal{A} = \{\vec{x} \in \Omega_h : \varphi(\vec{x}) > 0\}$ ,
- the void region:  $\mathcal{B} = \{\vec{x} \in \Omega_h : \varphi(\vec{x}) < 0\}$ ,
- and the immersed boundary:  $\mathcal{I} = \{\vec{x} \in \Omega_h : \varphi(\vec{x}) = 0\}$

as can be seen in fig. 4.1. In our next step, we use the definitions above in (3.8) considering

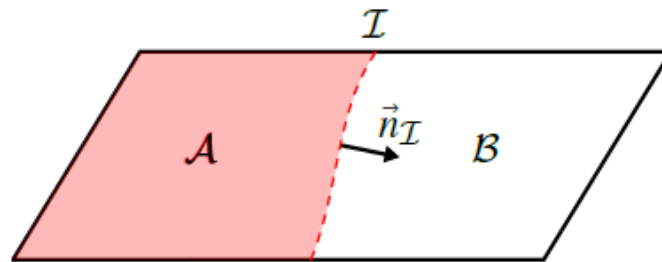


**Figure 4.1.:** Cut cell with physical (red) and void region (white) [9]

cell  $\mathcal{K}_i$  with the sub-domain  $\mathcal{A}_i = \mathcal{K}_i \cap \mathcal{A}$  and the surface  $\partial \mathcal{A}_i$ . As in cut cells the surface

$\partial \mathcal{A}_i$  consists not only of the edges  $\{\mathcal{E}_{i,e}^{\mathcal{A}}\}_{e=1,\dots,E} = \{\mathcal{E}_{i,e} \cap \bar{\mathcal{A}}_i\}_{e=1,\dots,E}$ , but also of the boundary segment  $\mathcal{J}_i = \mathcal{K}_i \cap \mathcal{J}$ , the discrete weak formulation using an IBM follows as

$$\int_{\mathcal{A}_i} \frac{\partial c_i}{\partial t} \Phi_{i,j} dV + \sum_{e=1}^{E_i} \int_{\mathcal{E}_{i,e}^{\mathcal{A}}} f(c^-, c^+, \mathbf{n}) \Phi_{i,j} dA + \int_{\mathcal{J}_i} f(c^-, c^+, \mathbf{n}_{\mathcal{J}}) \Phi_{i,j} dA - \int_{\mathcal{A}_i} \mathbf{f}(c_i) \cdot \nabla \Phi_{i,j} dV = 0 \quad (4.1)$$

with  $\mathbf{n}_{\mathcal{J}} = -\frac{\nabla \varphi}{\|\nabla \varphi\|}$ . In intersected cells the mass matrix is defined by

$$(\mathbf{M}_i)_{k,j} := \int_{\mathcal{A}_i} \Phi_{i,k} \Phi_{i,j} dV \quad (4.2)$$

and the discrete operator by

$$(\mathbf{f}_i)_j := \sum_{e=1}^{E_i} \int_{\mathcal{E}_{i,e}^{\mathcal{A}}} f(c^-, c^+, \mathbf{n}) \Phi_{i,j} dA + \int_{\mathcal{J}_i} f(c^-, c^+, \mathbf{n}_{\mathcal{J}}) \Phi_{i,j} dA - \int_{\mathcal{A}_i} \mathbf{f}(c_i) \cdot \nabla \Phi_{i,j} dV. \quad (4.3)$$

The difficulty of the IBM lies in the correct evaluation of  $\mathcal{A}_i$  and  $\mathcal{J}_i$  and in the agglomeration of intersected cells with very small volume fractions

$$\text{frac}(\mathcal{A}_i) = \frac{\text{meas}(\mathcal{A}_i)}{\text{meas}(\mathcal{K}_i)} \quad (4.4)$$

as we will discuss in section section 4.3.

---

## 4.2 RK Time Discretisation with Immersed Boundaries

---

In this thesis we only use explicit Euler time discretisation for immersed boundary problems as we are only interested in the steady state:

$$\mathbf{c}_i(t_1) = \mathbf{c}_i(t_0) - \Delta t \mathbf{M}_i^{-1} \mathbf{f}_i(c). \quad (4.5)$$

Using IBMs, we have to modify the stability criterion and therefore use the modified step restriction

$$\Delta t \leq \frac{c_{CFL}}{2P+1} \frac{\sqrt[p]{\text{meas}(\mathcal{A}_i)}}{\|\mathbf{u}\| + \alpha} \quad (4.6)$$

which is strongly influenced by the sub-cell  $\mathcal{A}_i$  with the smallest volume.

### 4.3 Cell Agglomeration

As can be seen in equation (4.6), the time step size is strongly restricted in cells with very small volume fractions. This leads to an elongated calculation process thus rendering the method impractical. Therefore we need to agglomerate those small cells to larger ones using a cell agglomeration factor  $0 \leq \alpha \leq 1$ .

The cell agglomeration strategy depends on finding the source cells  $\{\mathcal{K}_s^{\text{src}}\}_{s=1,\dots,S}$  with  $\text{frac}(\mathcal{A}_i) \leq \alpha$  and agglomerating them to the neighbouring cell with the highest volume fraction, namely target cell  $\mathcal{K}_s^{\text{tar}}$ . In fig. 4.2 you can see the cell agglomeration for a smaller (b) and a bigger (c) agglomeration factor.

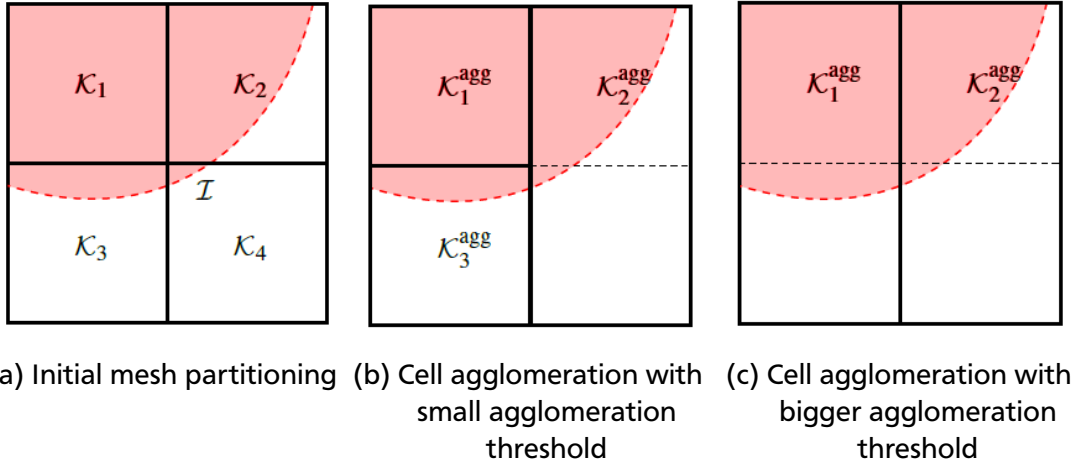


Figure 4.2.: Cell agglomeration, taken from [9]

For the neighbouring cells are weakly coupled via fluxes, the basis  $\vec{\Phi}_i$  can be extended from the target cell into the source cell. Therefore the source cell can formally be deleted from the discretisation mesh, reducing it to  $\{\mathcal{K}_s^{\text{agg}}\}_{i=1,\dots,N-S}$ . As can be found in MÜLLER, KRÄMER-EIS, KUMMER, *et al.* [9], it however does not reflect the actual implementation in BoSSS which only requires few cell-local matrix-vector products per time-step, thus not affecting the parallel efficiency.

### 4.4 Simulation Parameters Concerning Stability and Runtime in BoSSS

In the following, we will describe some of the preferences for the CNS solver that can be modified in order to stabilise the computations.



---

### LevelSetQuadratureOrder

The first preference is the *LevelSetQuadratureOrder*. It describes the quadrature order that is used for the evaluation of volume and edge operators. It is set to an integer; we will use a constant

```
c.LevelSetQuadratureOrder = 8;
```

in chapter 5 as it is important to have comparable results for the verification and a degree dependent order

```
c.LevelSetQuadratureOrder = 3*dgDegree;
```

in chapter 6 as it is more important to produce efficient and fast though stable results.

### SIPGPenaltyConstant

The second preference that we used is the *SIPGPenaltyConstant*. It is set to a double that should be greater than one and describes the weighting of the viscous terms. For the stability of the computation it is essential that the numerical flux functions that are used for the discretisation of the viscous terms are consistent. This can be achieved by different methods; one of those being the *Symmetric Interior Penalty Method (SIPG)* which introduces the penalty factor. In chapter 6, we will set

```
c.SIPGPenaltyConstant = 5.0;
```

for our calculations.

### NodeCountSafetyFactor

The last factor that we will vary for a better stability, is the *NodeCountSafetyFactor*. This factor, that is also set to a double, indicates the number of the nodes with respect to the number of modes that will be used during the quadrature. By standard, *BoSSS* sets it to 1.0; in our calculations we mostly used a *NodeCountSafetyFactor* of 2.0 in chapter 5 and of 5.0 in chapter 6, though it has been modified for few calculations in order to get them more stable.

All of these factors should be set just high enough in order to ensure a accurate and stable solution and the shortest possible runtime at the same time.

---

## 5 Verification of BoSSS for Inviscid Flows

In the following chapter, we will regard a flow at Mach 0.2 around a frictionless cylinder with adiabatic slip walls at changing parameters. We will compute a domain with  $-40 \leq x \leq 40$ ,  $0 \leq y \leq 40$ , a cylinder radius of  $r = 1$  and the consequential level set  $\varphi = x^2 + y^2 - 1$ . We are only considering the upper half of the domain as we can assume a symmetric flow.

For we will regard an isentropic inviscid flow with

$$\frac{p}{\rho^\gamma} = \text{const} \quad (5.1)$$

we can compare our results for the entropy to the analytical solution  $s = 0$ . Using this comparison we aim at verifying **BoSSS** for inviscid flows and **IBMs** considering robustness and convergence.

---

### 5.1 Robustness Study

---

In the first study regarding the frictionless cylinder, we compare the absolute error of entropy for a polynomial degree from 1 to 3 along a shift of the centre point of the cylinder from  $-0.075$  to  $0.075$  at steps of  $0.015$ . Therefore the level set  $\varphi$  will now be described by  $\varphi = (x - \text{shift})^2 + y^2 - 1^2$ . By shifting the cylinder, we can consider several cases where the cells would be cut differently and therefore cause different cell agglomerations. The cell agglomeration threshold is at a constant level of  $0.5$  in a mesh of  $64 \times 64$  cells (see fig. A.1) thus causing different cell agglomerations with every shift. In this example, we aim at proving the robustness of the solver, as for each position of the cylinder the error of entropy should not vary too much, thus making it independent of the way the border cells are cut.

As we look at fig. 5.1, first of all we note that the absolute error of entropy decreases with increasing polynomial degree. As a higher degree implies a better approximation, this can be explained very easily.

Secondly, we can observe that the error of entropy behaves roughly symmetrically to the ordinate which is unsurprising as we shifted the cylinder symmetrically.

For degree 1 and 2, the error is at a fairly constant value throughout the cylinder shift; at the polynomial degree 3 it is very irregular. The two most discordant values appear at a shift of  $\pm 0.03$ . There the calculation was very unstable. By varying the parameters explained in

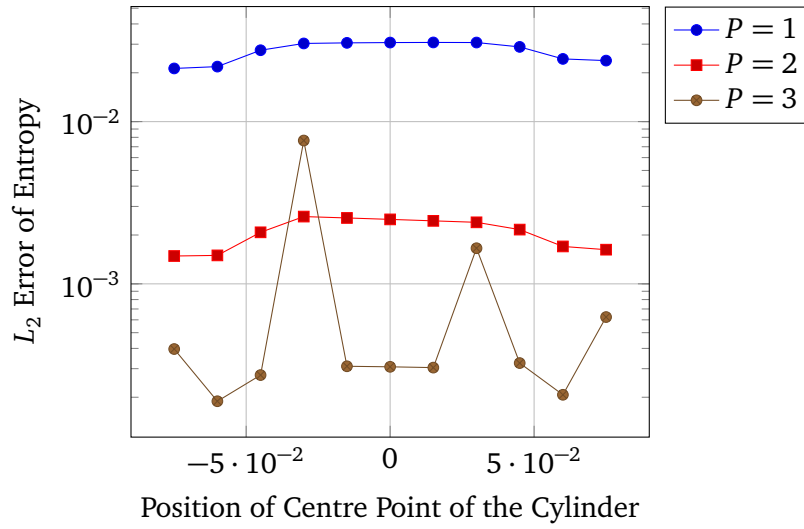
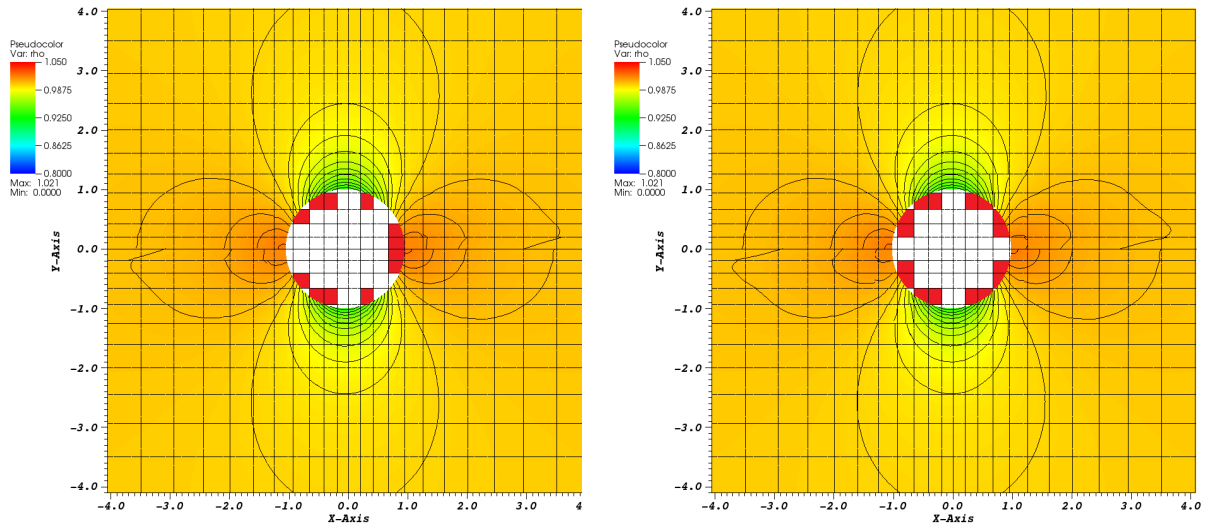


**Figure 5.1.: Convergence Plot**

section 4.4, we made them as stable as possible but still produced the inaccurate values shown in fig. 5.1.

We can therefore infer that with increasing polynomial degree at a mesh that coarse the calculation gets very unstable; a finer mesh should be used.

Now we will consider the two cases which have the largest error difference apart from degree 3 - degree 2 at the shifts  $-0.06$  and  $-0.03$  - more closely.



**Degree 2, shift  $-0.06$**

**Degree 2, shift  $-0.03$**

**Figure 5.2.: Isolines of pressure**

---

In fig. 5.2 you can see the two mentioned cases with highlighted isolines of pressure and pseudocoloured density. As only the upper half of the cylinder has been calculated, we reflected the results through the centre point of the cylinder. Therefore you can easily see that the results are not flawless, as the flow before and after the obstacle should be identical. Furthermore you can see that in the left picture the isolines are smoother than in the right one. We also highlighted the cells that have been agglomerated in red; in the right case almost every cut cell has been agglomerated while in the left one it were fewer. It may be assumed that each agglomeration causes an error which results into the higher error that we observed in fig. 5.1. Unfortunately we did not find a proper explanation for the agglomeration error; this could be subject of future research.

Except for the polynomial degree 3, the error of entropy changes very little for the different cases. We can therefore assume that the solver is good enough validated concerning the way the agglomerated cells influence the calculation as long as we consider a fine enough mesh for higher degrees.

---

## 5.2 Convergence Study of Mesh Size and Polynomial Degree

---

In the second study, we vary the mesh size of our geometry from  $32 \times 32$  by  $64 \times 64$  to  $128 \times 128$  cells. Additionally, we also vary the polynomial degree from 0 to 4, consequently regarding fifteen cases in total. The agglomeration factor is at a constant moderate level  $\alpha = 0.3$ . Our aim is the validation of the convergence of the RKDG method based solver for the inviscid cylinder. Therefore we hope to achieve an experimental order of convergence that is near the optimal rate  $\mathcal{O}(h^{P+1})$ . In fig. 5.3, we compared the absolute error entropy to the mesh size logarithmically for each polynomial degree and added the linear regressions  $R_P$  with its slopes to each graph.

As you can see in fig. 5.3, each graph has a quite constant slope that is higher with increasing polynomial degree. For  $1 < P < 4$  it is approximately of the order  $P + 1$  as we hoped, only for  $P = 0$  the computations converge much more slowly.

Again it was necessary to adjust some of the parameters explained in section 4.4 in order to stabilise the calculations with higher polynomial degrees.

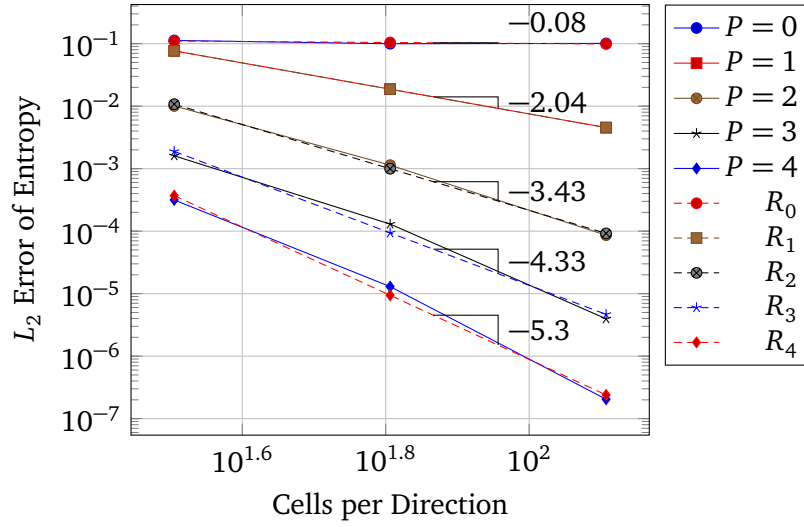


**Figure 5.3.:** Convergence Plot

As an example for the correction of a critical calculation, we visualised the case with mesh size  $128 \times 128$  and polynomial degree  $P = 3$  before and after the correction in fig. 5.4. Again, we visualised entropy and pressure. The picture in the middle shows a zoomed view of the critical cell where a high amount of entropy was produced and lead to the breakup. Please remark that differently coloured entropy ranges had to be used before and after the correction in order to point out the critical cell.

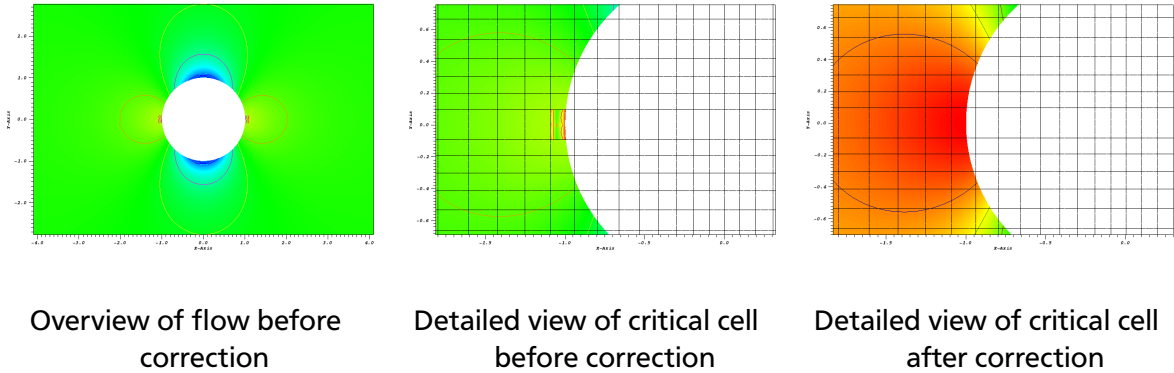


**Figure 5.4.:** Mesh size  $128 \times 128$ ,  $P = 3$

### 5.3 Conclusion

After having studied the behaviour of BoSSS concerning the Euler equations with immersed boundaries, we can conclude that it is sufficiently verified. The robustness study showed that the results are mostly independent from the exact position of the grid cells. During the convergence study we remarked that the convergence behaves as desired with an order close to the optimal rate of  $\mathcal{O}(h^{P+1})$ .

---

Nevertheless in order to receive the correct results one sometimes needs to put a large effort into adjusting parameters for stable calculations.

---

## 6 Evaluation of BoSSS for Viscid Flows

In this chapter, we aim at validating BoSSS for viscid flows with IBMs. In order to have a good comparable result, we will once again regard the flow around a cylinder as in chapter chapter 5. The viscous flow around a cylinder has been approached by many papers both experimentally and numerically, e.g. WILLIAMSON [10], PERSILLON and BRAZA [11], CANUTO and TAIRA [12], though very few numerical approaches use a RKDG method combined with immersed boundaries. In order to validate the BoSSS code with immersed boundaries not only for the Euler equations as we did in chapter chapter 5 but also for the viscous case we will now consider different Reynolds numbers for the steady and unsteady flow and compare our results to those of other studies.

---

### 6.1 Theory

---

The flow around a viscous cylinder can be divided into different sections depending on the Reynolds number as shown in fig. 6.1. The first section applies for Reynolds numbers  $0 < Re < 40 - 50$  characterised by a laminar steady flow. In that regime, a recirculation region with two symmetric vortices with opposite directions is comprised by the wake. The flow can be described using the wake separation length  $W^*$ .

The second section contains all other Reynolds number  $Re > 40 - 50$  and thus describes the unsteady flow. It can be subdivided in several subsections [10]:

- $40 - 50 < Re < 190$ : laminar vortex shedding,
- $190 < Re < 260$ : 3D wake-transition regime,
- $260 < Re < 1000$ : increasing disorder in the fine-scale three-dimensionalities,
- $1000 < Re < 200000$ : shear layer transition regime,
- $200000 < Re$ : critical transition, supercritical regime and post-critical regime.

As we will only discuss Reynolds numbers up to  $Re = 200$ , the important phases for us are the laminar steady regime and the laminar vortex shedding. At around  $Re = 190$ , the three dimensionality of the system has an incrementing influence on the flow; for we only analyse the 2D model of the experiment we stop at  $Re = 200$  expecting slight deflection in our results.

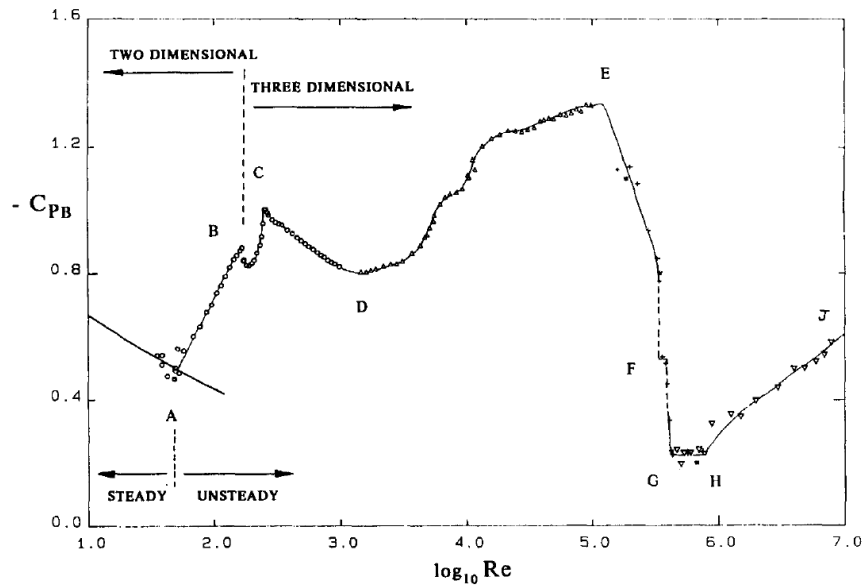
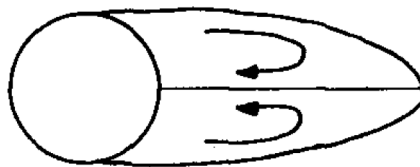


**Figure 6.1.:** Overview of Base Suction Coefficients over Reynolds Number [10]

### 6.1.1 The Laminar Steady Regime

At Reynolds numbers below 50, the flow forms a steady recirculation region, characterised by the wake separation length  $W^*$ . It is built by two symmetrically placed vortices on each side of the wake as can be seen in fig. 6.2. It has been shown experimentally as well as numerically that the wake separation length increases with increasing Reynolds number.



**STEADY WAKE**

**Figure 6.2.:** Recirculation Region [10]

### 6.1.2 Laminar Vortex Shedding

For Reynolds numbers of between 50 and 200 the recirculation region develops instabilities leading to the development of turbulence in the wake. This results into fully periodic vortex shedding, known as the Kármán vortex street, as can be seen in fig. 6.3. With increasing Reynolds number the amplitudes of the drag and lift coefficients increase while the Strouhal number and frequency, respectively, decrease.



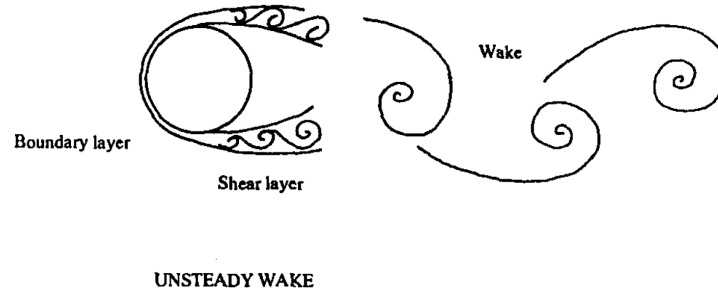


**Figure 6.3.:** Kármán Vortex Street [10]

## 6.2 Simulations

In this section we will compare the lift and drag coefficients  $C_L$  and  $C_D$  at different Reynolds numbers and mesh sizes at a constant agglomeration threshold of 0.3, different polynomial degrees of 1, 2 and 3 and meshes of  $40 \times 40$ ,  $60 \times 60$  and  $80 \times 80$  cells. The meshes can be found in the appendix.

The different simulation properties will be abbreviated as DG + *polynomial degree* + CpD + *number of cells per direction*, e.g. DG2CpD80 for a simulation with polynomial degree 2 and  $80 \times 80$  cells.

In table 6.1 you can see the total **Degrees of Freedom (DoF)** for each simulation taking into account the **DoFs** produced by order 1, 2 and 3 with 3, 6 and 10 **DoFs** per cell.

DoF		CpD		
		40	60	80
DG	1	4800	10800	19200
	2	9600	21600	38400
	3	16000	36000	64000

**Table 6.1.:** Degrees of Freedom for Different Simulation Properties

During the evaluation of our results, we will also compare simulations of similar **DoFs** like DG2CpD40 and DG1CpD60 or DG3CpD60 and DG2CpD80 in order to inspect the influence of higher order and finer mesh properties.

The drag and lift coefficients are defined as

$$C_D = \frac{d}{q_\infty L_\infty} \quad (6.1)$$

$$C_L = \frac{l}{q_\infty L_\infty} \quad (6.2)$$

---

with the dynamic pressure  $q_\infty = \frac{1}{2}\rho_\infty V_\infty^2$ . For we set  $L_\infty = \rho_\infty = V_\infty = 1$  in our boundary and initial conditions, we can assume

$$C_D = 2 \cdot d \quad (6.3)$$

$$C_L = 2 \cdot l, \quad (6.4)$$

with the drag and lift forces  $d$  and  $l$  provided from the calculation.

As we expect asymmetrical oscillations of the flow with higher Reynolds numbers, we cannot limit the domain to the upper or lower half as we did in chapter 5. In order to reduce the runtime of the calculations, we will compute a smaller domain with  $-20 \leq x \leq 20$ ,  $-20 \leq y \leq 20$  and the cylinder radius  $r = 0.5$  during the simulations. We will use a rectangular mesh that is finer near the cylinder with the level set  $\varphi = x^2 + y^2 - 0.5^2$ , an isothermal wall boundary condition at the cylinder wall and supersonic inlet boundary conditions for the domain borders that shall prevent the reflection of the initial wave.

---

### 6.2.1 Steady State Simulations ( $\text{Re} < 40 - 50$ )

---

For the steady state simulations, we can use the wake separation length  $W^*$  as an additional variable to compare to other simulations. It can be found from examining the x-velocity  $U$  at

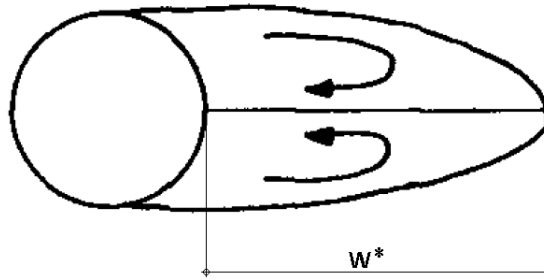


**Figure 6.4.:** Wake separation length, taken from [10], modified

$y = 0$ ; the x-position where  $U$  changes its sign should be the end position of the wake.

---

#### Simulation at Reynolds Number 20

---

We will now simulate the flow at  $\text{Re} = 20$  and compare our results to several experimental and numerical results as shown in table 6.2. The results are divided into three categories: experimental, numerical incompressible and numerical compressible in order to coincide with the arrangement given by AYERS [2]. Furthermore the results are divided into 2D and 3D simulations

which should not produce large differences as long as we are regarding low Reynolds numbers. The values that were produced by BREHM, HADER, and FASEL [18] using  $Ma = 0.1$  as well as those that were simulated as incompressible flows can still be compared as in these low Mach numbers the compressibility does not have a great effect on the flow.

Re = 20	Source	2D/3D	$W^*$	$C_D$
Numerical – Incompressible	DENNIS and CHANG [13]	2D	0.94	2.05
	FORNBERG [14]	2D	0.91	2.00
	LINNICK and FASEL [15]	2D	0.93	2.06
Experimental	COUTANCEAU and BOUARD [16]	-	0.93	-
	TRITTON [17]	-	-	2.09
Numerical – Compressible	BREHM, HADER, and FASEL [18] ( $Ma = 0.1$ )	3D	0.96	2.02
	AYERS [2]	2D	0.975	2.06
	<b>Present Results:</b>	2D	0.928	2.136

**Table 6.2.:** Comparison of Results for  $W^*$  and  $C_D$ , taken from [2], modified

For the comparison of our values, we will take the results of our best simulation DG3CpD60. As we can see in table 6.2, the values for the coefficient of drag are in pretty good agreement though they show a tendency of being too high. The simulated wake separation length is very accurate.

In tables 6.3 and 6.4 you can see all of the results that we got by our simulations.

$C_D$		CpD		
		40	60	80
DG	1	1.812	1.952	1.988
	2	2.141	2.138	2.197
	3	2.136	2.136	-

**Table 6.3.:**  $C_D$  Values for Each Simulation (Re = 20)

$W^*$		CpD		
		40	60	80
DG	1	0.956	1.044	0.927
	2	0.887	0.943	0.916
	3	0.921	0.928	-

**Table 6.4.:** Wake Separation Lengths for Each Simulation (Re = 20)

We did not simulate DG3CPD80 as it would have taken much longer, being the simulation on the finest mesh with the highest order, than the other simulations. What is striking about our values is the discordant value of DG2CpD80 which should have been the most accurate simulation. Figure 6.5 graphically presents the values of table 6.3 and shows that higher degrees produce much faster accurate results than finer meshes.

In fig. 6.6 you can see the behaviour of the coefficient of drag over time for different sim-

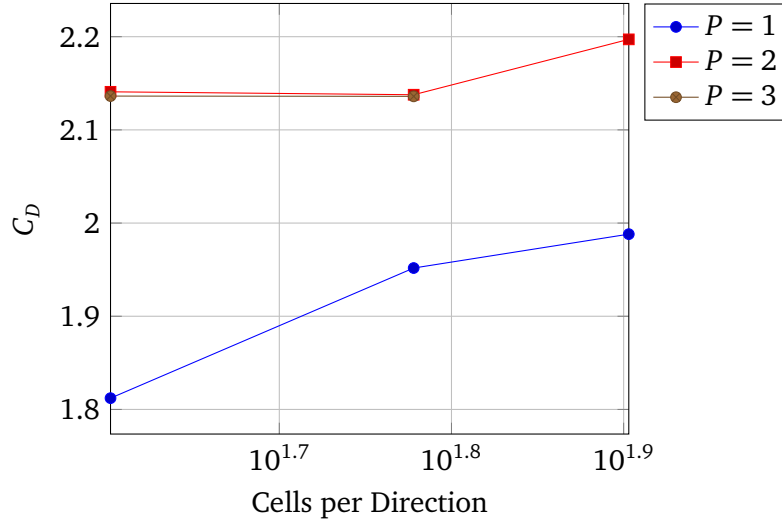


**Figure 6.5.:** Graphical Presentation of Table 6.3 for  $Re = 20$

ulations. The peak at the beginning is produced because the flow reacts to the cylinder that is suddenly put into place at  $t = 0$ . Afterwards the value drops quickly; at around  $t = 10$  the almost steady state is reached, though the  $C_D$  value is still slightly falling. We stopped the simulation at  $t = 14$  so we could better compare the result to the one of AYERS [2]. It is to be assumed that for a longer simulation time the flow would reach the completely steady state and the coefficient of drag would finally converge to the expected value. The examination of its behaviour for a longer simulated physical time shall be subject of future works.

We will conclude the examination of the flow for  $Re = 20$  with the visualisation of the vorticity for DG3CpD60 in fig. 6.7.

---

### Simulation at Reynolds Number 40

---

As we did for  $Re = 20$ , we will now compare our results for the wake separation length and the coefficient of drag to those documented before by others. Once again, we compare our result simulated with DG3CpD60 which now is much more accurate than it was for  $Re = 20$ . Both the coefficient of drag and the wake separation length are in very good agreement with the other values; the coefficient of drag is slightly higher while the wake separation length is slightly lower than the results we are comparing to. As we expected before, we can confirm the theory that higher Reynolds number cause higher wake separation lengths. In tables 6.6 and 6.7, you can see the results of every simulation. As we did for  $Re = 20$ , we did not simulate

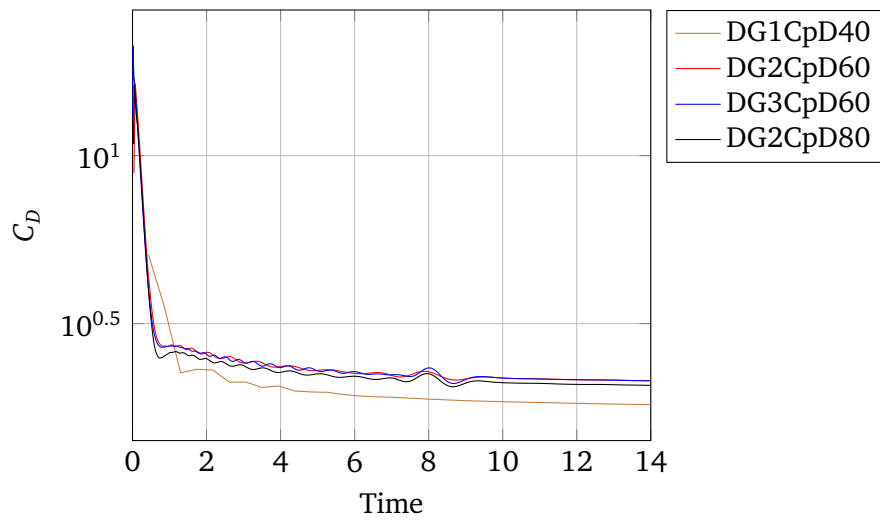


**Figure 6.6.:** Coefficient of Drag over Time ( $Re = 20$ )

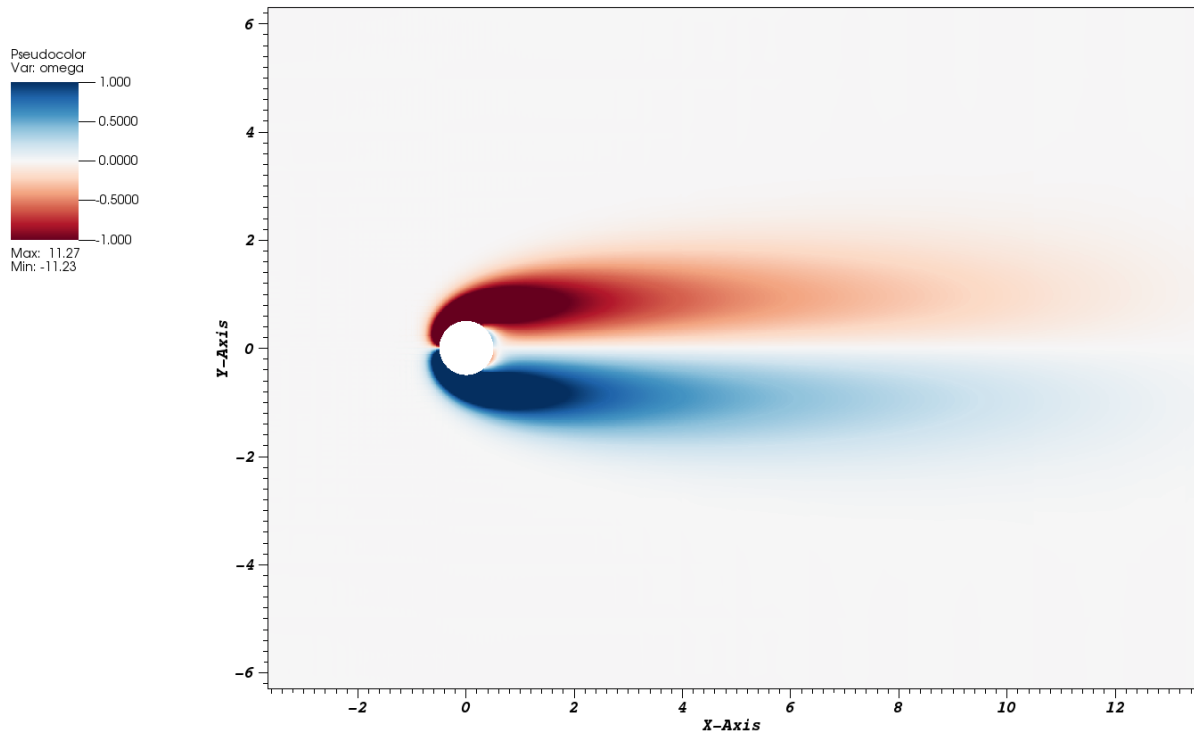


**Figure 6.7.:** Vorticity for DG3CpD60 for  $Re = 20$

Re = 40	Source	2D/3D	$W^*$	$C_D$
Numerical – Incompressible	DENNIS and CHANG [13]	2D	2.35	1.52
	FORNBERG [14]	2D	2.24	1.50
	LINNICK and FASEL [15]	2D	2.28	1.54
Experimental	COUTANCEAU and BOUARD [16]	-	2.13	-
	TRITTON [17]	-	-	1.59
Numerical – Compressible	BREHM, HADER, and FASEL [18] (Ma = 0.1)	3D	2.26	1.51
	AYERS [2]	2D	2.250	1.605
	<b>Present Results:</b>	2D	2.201	1.608

**Table 6.5.:** Comparison of Results for  $W^*$  and  $C_D$ , taken from [2], modified

DG3CpD80 as it would have taken too long. Unfortunately, we did not get a stable calculation for DG3CpD40 until we reduced the time step by ninety-five per cent. This resulted into a tremendous runtime which made the simulation impossible.

In fig. 6.8 you can see the graphical presentation of table 6.6; here it is very clear that higher

$C_D$		CpD		
		40	60	80
DG	1	1.373	1.461	1.485
	2	1.600	1.596	1.616
	3	-	1.608	-

**Table 6.6.:**  $C_D$  Values for Each Simulation (Re = 40)

$W^*$		CpD		
		40	60	80
DG	1	2.342	2.338	2.236
	2	2.115	2.182	2.182
	3	-	2.201	-

**Table 6.7.:** Wake Separation Lengths for Each Simulation (Re = 40)

order calculations provide even for coarse meshes very accurate solutions.

As you can see in fig. 6.9, the behaviour of the coefficient of drag over the physical time is very similar for the simulations plotted. They are more in agreement with each other than they were for Re = 20. In fig. 6.10, you can see the vorticity for DG3CpD60; there we remark that the wake is much longer than it was for Re = 20.

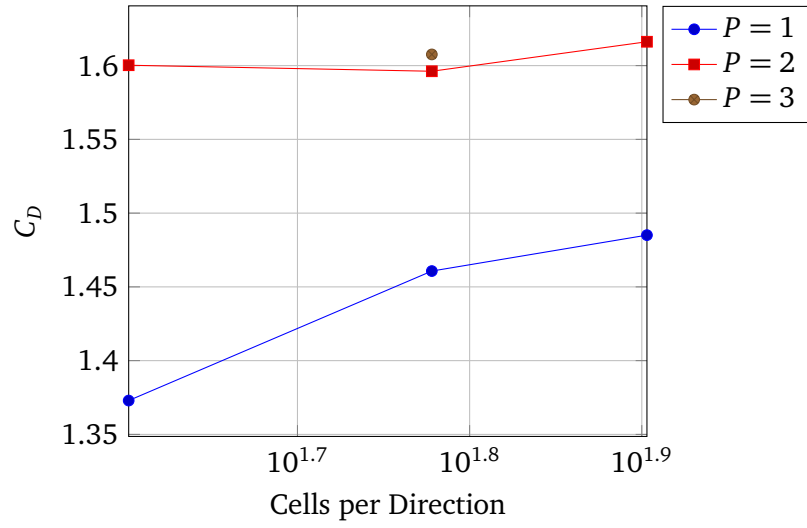


**Figure 6.8.:** Graphical Presentation of Table 6.6 for  $Re = 40$

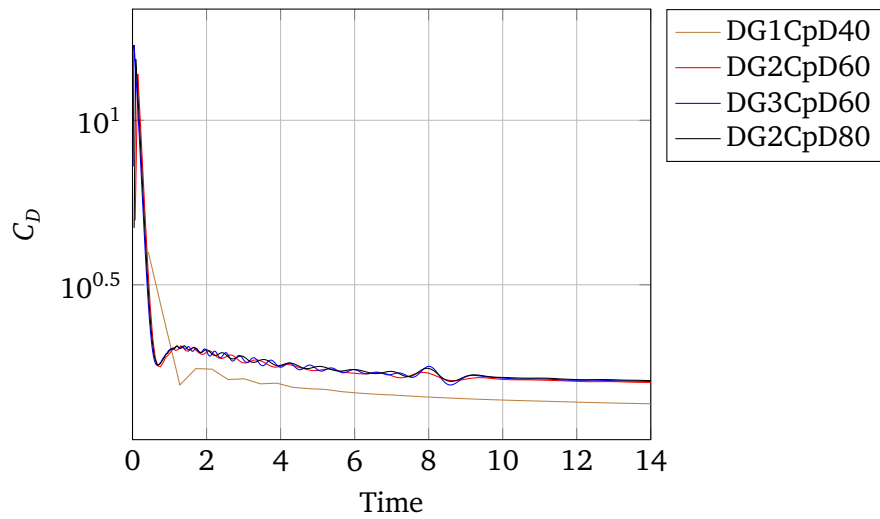


**Figure 6.9.:** Coefficient of Drag over Time ( $Re = 40$ )

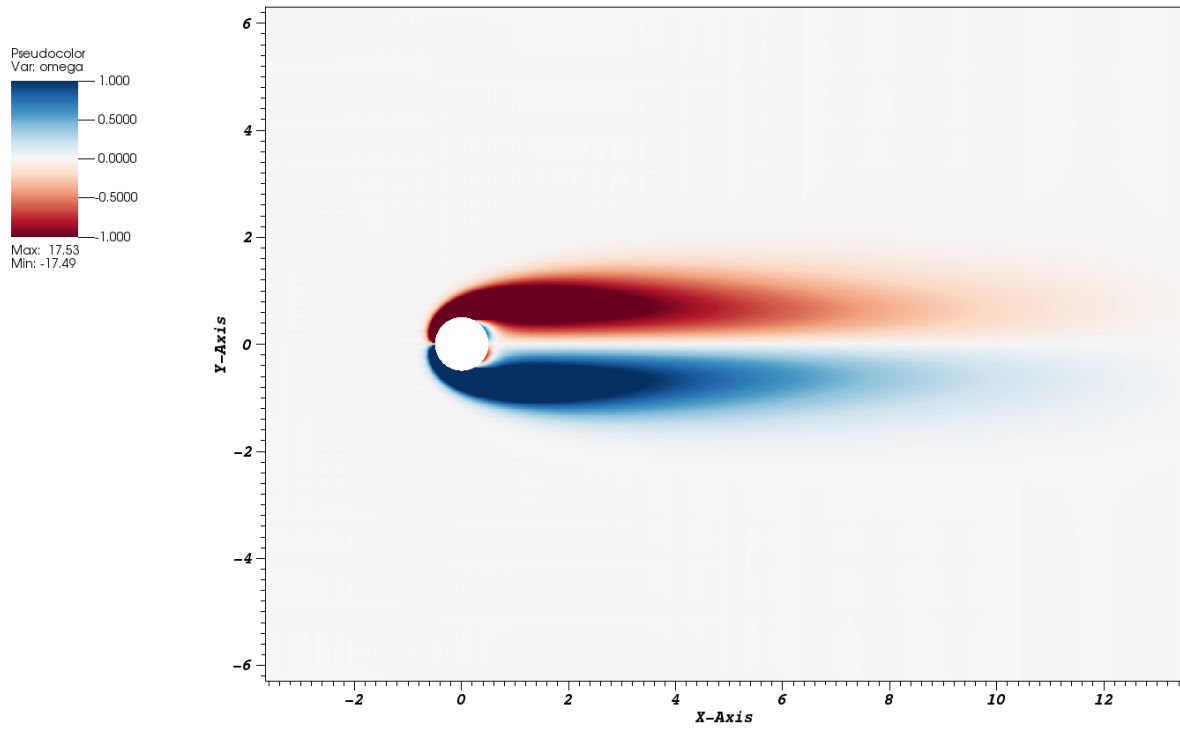


**Figure 6.10.:** Vorticity for DG3CpD60 for  $Re = 40$

### 6.2.2 Unsteady Simulations ( $Re > 40 - 50$ )

After having examined the steady simulations which were very accurate for the coefficient of drag, we will now turn to the unsteady ones with  $Re = 100$  and  $Re = 200$ . In order to compare the unsteady simulations, we need the Strouhal number

$$St = \frac{f L_{\infty}}{V_{\infty}}. \quad (6.5)$$

As our initial and boundary conditions give  $V_{\infty} = L_{\infty} = 1$ , we can calculate  $St = f$  with  $f$  found from examining the oscillation of  $C_L$  over time. In order to develop vortex shedding, the flow needs small perturbations that destabilise the flow towards a symmetry breaking state (PERSILLON and BRAZA [11]). In reality those are given by the structure of the cylinder, the influence of the walls or the not completely straight inflow; in our simulations they come from small truncation errors and the computer's round-off errors. In order to accelerate the process until the wake begins to oscillate, one could also start the flow with a vortex that induces a high perturbation much earlier. For it did not take long until the wake began to oscillate it was not needed in our simulations.



---



---

## Simulation at Reynolds Number 100

---

In the following, we will compare the coefficients of lift and drag as well as the Strouhal number. As you can see in table 6.8, the produced results are once again very accurate and in good agreement with those of other studies. All of our results for the best calculation DG3CpD60 lie perfectly in the range that has been given by other studies. The overview of all collected values can be found in tables 6.9 to 6.11. They are written as mean value plus/minus amplitude in order to show the oscillation of lift and drag. We can clearly observe that DG1CpD40 produces very inaccurate results; as soon as either mesh fineness or **DG** order is increased, we immediately receive very good results. Furthermore we observe that the higher-order results of those with the same **DoFs** yield better results than those with a finer mesh.

Re = 100	Source	2D/3D	$St$	$C_D$	$C_L$
Numerical – Incompressible	GRESHO, CHAN, LEE, <i>et al.</i> [19]	2D	0.18	1.76	-
	LINNICK and FASEL [15] ( $\lambda = 0.056$ )	2D	0.169	$1.38 \pm 0.010$	$\pm 0.337$
	LINNICK and FASEL [15] ( $\lambda = 0.023$ )	2D	0.1696	$1.34 \pm 0.009$	$\pm 0.333$
	PERSILLON and BRAZA [11]	2D	0.165	1.253	-
	SAIKI and BIRINGEN [20]	2D	0.171	1.26	-
	PERSILLON and BRAZA [11]	3D	0.164	1.240	-
	LIU, ZHENG, and SUNG [21]	3D	0.165	$1.35 \pm 0.012$	$\pm 0.339$
Experimental	BERGER and WILLE [22]	-	0.16 – 0.17	-	-
	CLIFT, GRACE, and WEBER [23]	-	-	1.24	-
	WILLIAMSON [10]	-	0.164	-	-
Numerical – Compressible	BREHM, HADER, and FASEL [18] ( $Ma = 0.1$ )	3D	0.165	$1.32 \pm 0.01$	$\pm 0.32$
	AYERS [2]	2D	0.167	$1.371 \pm 0.011$	$\pm 0.333$
	<b>Present Results:</b>	2D	0.1669	$1.3593 \pm 0.00805$	$\pm 0.3291$

**Table 6.8.:** Comparison of Results for  $St$ ,  $C_D$  and  $C_L$ , taken from [2], modified

$C_D$		CpD		
		40	60	80
DG	1	$0.9777 \pm 0.0003$	$1.2 \pm 0.0834$	$1.233 \pm 0.0118$
	2	$1.291 \pm 0.0082$	$1.3156 \pm 0.0089$	$1.3501 \pm 0.0079$
	3	-	$1.3593 \pm 0.00805$	-

**Table 6.9.:**  $C_D$  Values for Each Simulation (Re = 100)

$C_L$		CpD		
		40	60	80
DG	1	$\pm 0.00155$	$\pm 0.291$	$\pm 0.2789$
	2	$\pm 0.2672$	$\pm 0.3154$	$\pm 0.3135$
	3	-	$\pm 0.3291$	-

**Table 6.10.:**  $C_L$  Values for Each Simulation (Re = 100)

St		CpD		
		40	60	80
DG	1	0.1001	0.1506	0.1502
	2	0.1669	0.1669	0.1670
	3	-	0.1669	-

**Table 6.11.:** Strouhal Numbers for Each Simulation (Re = 100)

In fig. 6.11 the coefficient of lift over time is presented. It shows that at around  $t = 90s$  amplitude and frequency stay the same, though regarding fig. 6.13 the coefficient of drag reaches the constant oscillation state at around  $t = 110s$ . These plots were produced with the results from DG3CpD60. They also show that the frequency of  $C_D$  is twice as high as the frequency of the lift coefficient.

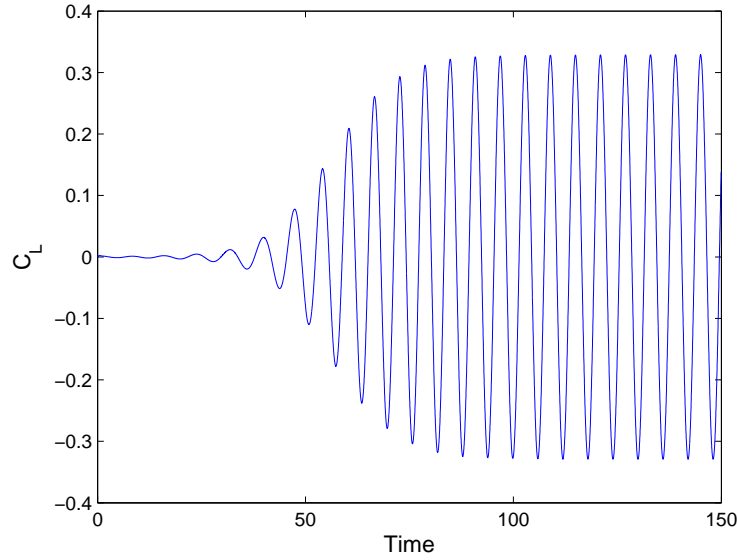


**Figure 6.11.:** Lift coefficient over time for  $0s < t < 150s$  ( $Re = 100$ )

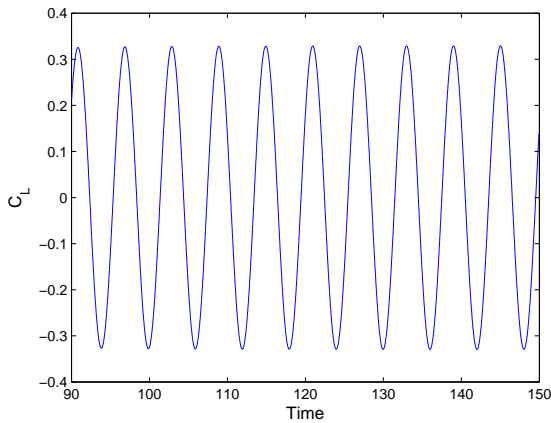


**Figure 6.12.:** Lift coefficient over time for  $90s < t < 150s$  ( $Re = 100$ )

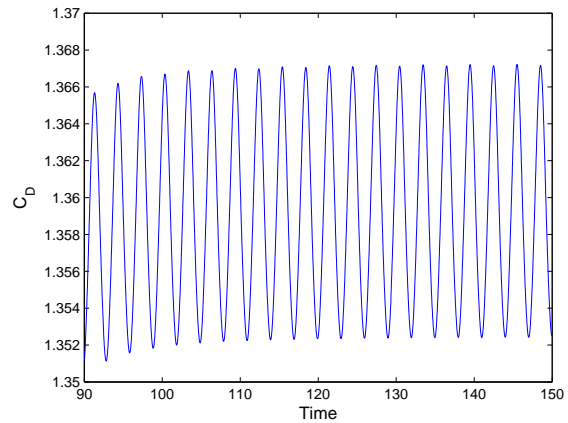


**Figure 6.13.:** Drag coefficient over time for  $90s < t < 150s$  ( $Re = 100$ )

We will conclude the evaluation of the simulation at Reynolds number 100 with a visualisation of the vorticity for DG2CpD60 in fig. 6.14. As we used a very coarse mesh outside  $-2 \leq x, y \leq 2$  the vortices get stretched in the wake and there are sharp jumps at the cell edges. By observing the vorticity over time, we could conclude that the Strouhal number, which describes

---

the frequency of the vortex shedding, can be found from examining the coefficient of lift as vortex shedding and lift changes appeared in the exact same frequency.

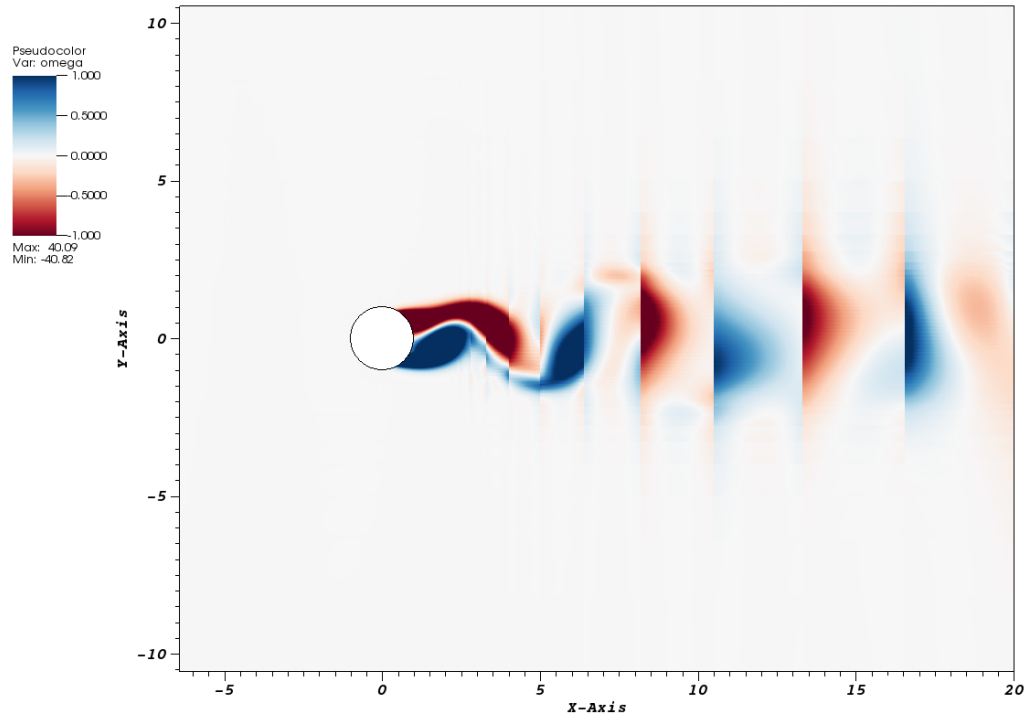


**Figure 6.14.:** Vorticity for DG3CpD60 for  $Re = 100$

---



---

### Simulation at Reynolds Number 200

---

Finally, we will come to the simulation at  $Re = 200$ . Once again, the results that we received are accurate and in good agreement, as can be seen in table 6.12. Compared to  $Re = 100$  the frequency of the vortex shedding as well as the amplitude of the coefficient of lift increased while the coefficient of drag stayed at about the same. Compared to the three dimensional simulations by BREHM, HADER, and FASEL [18], our results for the coefficient of drag are slightly higher, as we only did 2D simulations. All of our results can be found in tables 6.13 to 6.15.

Re = 200	Source	2D/3D	$St$	$C_D$	$C_L$
Numerical – Incompressible	BELOV, MARTINELLI, and JAMESON [24]	2D	0.193	$1.19 \pm 0.042$	$\pm 0.64$
	GRESHO, CHAN, LEE, <i>et al.</i> [19]	2D	0.21	1.76	-
	LINNICK and FASEL [15] ( $\lambda = 0.056$ )	2D	0.199	$1.37 \pm 0.046$	$\pm 0.70$
	LINNICK and FASEL [15] ( $\lambda = 0.023$ )	2D	0.197	$1.34 \pm 0.044$	$\pm 0.69$
	MIYAKE, SAKAMOTO, TOKUNAGA, <i>et al.</i> [25]	2D	0.196	$1.34 \pm 0.043$	$\pm 0.67$
	PERSILLON and BRAZA [11]	2D	0.198	1.321	-
	SAIKI and BIRINGEN [20]	2D	0.197	1.18	-
	PERSILLON and BRAZA [11]	3D	0.181	1.306	-
	LIU, ZHENG, and SUNG [21]	3D	0.192	$1.31 \pm 0.049$	$\pm 0.69$
Experimental	BERGER and WILLE [22]	-	0.18 – 0.19	-	-
	CLIFT, GRACE, and WEBER [23]	-	-	1.16	-
	WILLIAMSON [10]	-	0.181	-	-
Numerical – Compressible	BREHM, HADER, and FASEL [18] ( $Ma = 0.1$ )	3D	0.192	$1.3 \pm 0.04$	$\pm 0.66$
	AYERS [2]	2D	0.201	$1.371 \pm 0.011$	$\pm 0.70$
	<b>Present Results:</b>	2D	0.2002	$1.344 \pm 0.0462$	$\pm 0.6887$

**Table 6.12.:** Comparison of Results for  $St$ ,  $C_D$  and  $C_L$ , taken from [2], modified

$C_D$		CpD		
		40	60	80
DG	1	$0.8144 \pm 0.0028$	$1.2427 \pm 0.0281$	$1.2256 \pm 0.0309$
	2	$1.2508 \pm 0.0339$	$1.3593 \pm 0.0080$	$1.3501 \pm 0.0079$
	3	-	$1.344 \pm 0.0462$	-

**Table 6.13.:**  $C_D$  Values for Each Simulation (Re = 200)

$C_L$		CpD		
		40	60	80
DG	1	$\pm 3.2629 \cdot 10^{-5}$	$\pm 0.5304$	$\pm 0.2789$
	2	$\pm 0.5653$	$\pm 0.6433$	$\pm 0.6376$
	3	-	$\pm 0.6887$	-

**Table 6.14.:**  $C_L$  Values for Each Simulation (Re = 200)

St		CpD		
		40	60	80
DG	1	0	0.1836	0.1838
	2	0.2003	0.2002	0.2002
	3	-	0.2002	-

**Table 6.15.:** Strouhal Numbers for Each Simulation (Re = 200)

In fig. 6.15, we can see that the steady state is reached earlier compared to  $Re = 100$ ; the coefficient of lift settles into a state of constant amplitude and frequency at around  $t = 65s$ . Figures 6.16 and 6.17 show the frequency and amplitude of  $C_L$  and  $C_D$ , respectively, for the steady state from  $90s \leq t \leq 150s$ . There we can see that frequency and amplitude are higher compared to  $Re = 100$ .

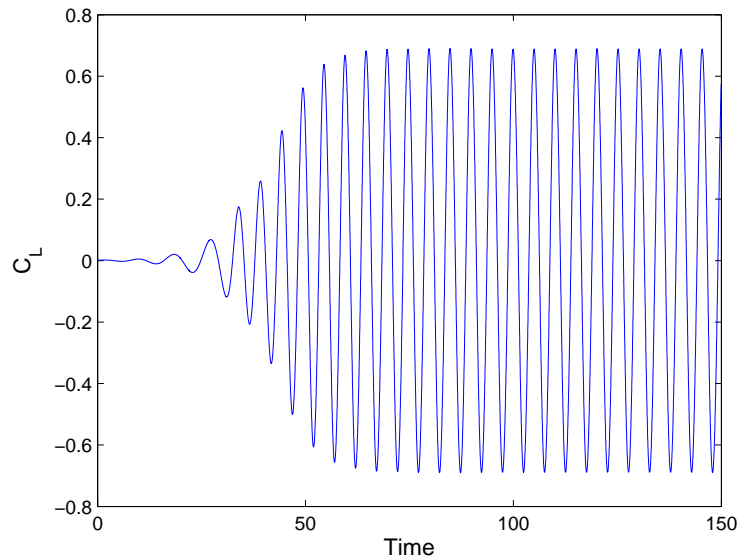


**Figure 6.15.:** Lift coefficient over time for  $0s < t < 150s$  ( $Re = 200$ )

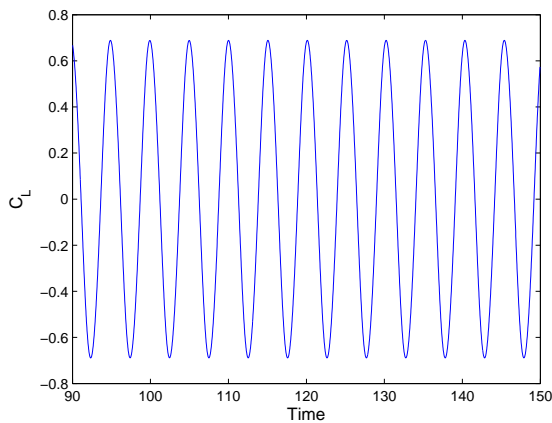


**Figure 6.16.:** Lift coefficient over time for  $90s < t < 150s$  ( $Re = 200$ )

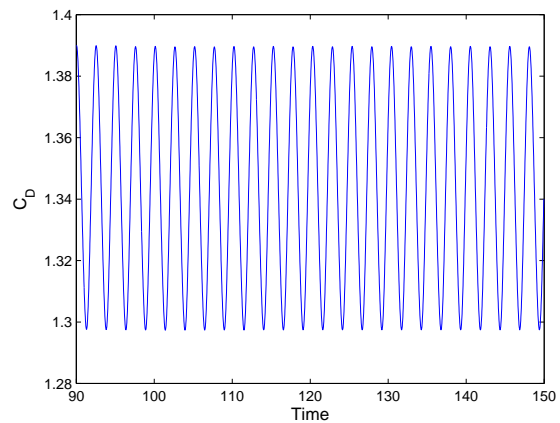


**Figure 6.17.:** Drag coefficient over time for  $90s < t < 150s$  ( $Re = 200$ )

---

We will conclude the simulation part of this work with the visualisation of the vorticity for  $Re = 200$  in fig. 6.18. We can observe that the amount of vortices has increased. Unfortunately the mesh is too coarse to properly show the wake of the cylinder.

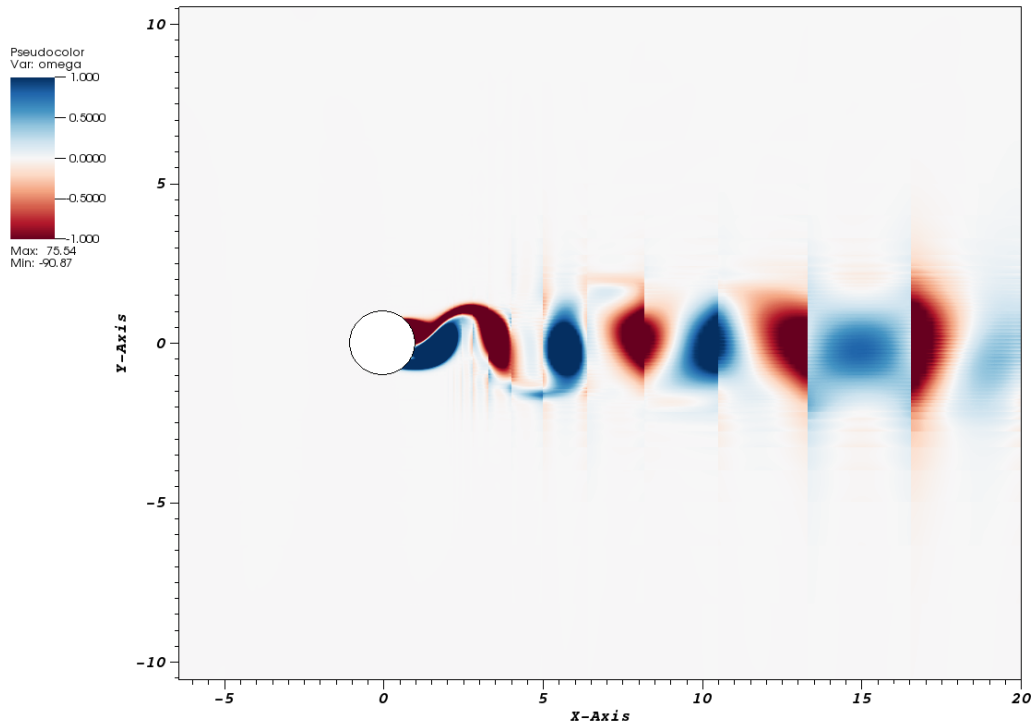


**Figure 6.18.:** Vorticity for DG3CpD60 for  $Re = 200$



---

## 7 Conclusion

---

## 8 Bibliography

- [1] MÜLLER, B., “Methods for higher order numerical simulations of complex inviscid fluids with immersed boundaries,” PhD thesis, TU Darmstadt, 2014.
- [2] AYERS, L. F., “Validation of a discontinuous galerkin based compressible cfd solver,” Bachelor thesis, Technische Universität Darmstadt, Dec. 2015.
- [3] KRÄMER-EIS, S., “Notes on the implementation of the viscous terms in cns: Code verification, fdy annual report 2014,” 2014.
- [4] COCKBURN, B., “Advanced numerical approximation of nonlinear hyperbolic equations: Lectures given at the 2nd session of the centro internazionale matematico estivo (c.i.m.e.) held in cetraro, italy, june 23–28, 1997,” in, QUARTERONI, A., Ed. Berlin, Heidelberg: Springer Berlin Heidelberg, 1998, ch. An introduction to the Discontinuous Galerkin method for convection-dominated problems, pp. 151–268, ISBN: 978-3-540-49804-9. DOI: 10.1007/BFb0096353.
- [5] TORO, E., “Riemann solvers and numerical methods for fluid dynamics. 2009,”
- [6] ENRIGHT, W., “The numerical analysis of ordinary differential equations: Runge-kutta and general linear methods (jc butcher),” 1989.
- [7] GOTTLIEB, S. and SHU, C.-W., “Total variation diminishing runge-kutta schemes,” *Mathematics of computation of the American Mathematical Society*, vol. 67, no. 221, pp. 73–85, 1998.
- [8] COCKBURN, B. and SHU, C.-W., “The runge-kutta local projection p1-discontinuous galerkin finite element method for scalar conservation laws,” *American Institute of Aeronautics and Astronautics*, vol. 25, no. 3, pp. 337–361, 1991.
- [9] MÜLLER, B., KRÄMER-EIS, S., KUMMER, F., *et al.*, “A high-order discontinuous galerkin method for compressible flows with immersed boundaries,” *International Journal or Numerical Methods in Engineering*, vol. 295, pp. 475–504, 2016, to be published.
- [10] WILLIAMSON, C. H., “Vortex dynamics in the cylinder wake,” *Annual review of fluid mechanics*, vol. 28, no. 1, pp. 477–539, 1996.
- [11] PERSILLON, H. and BRAZA, M., “Physical analysis of the transition to turbulence in the wake of a circular cylinder by three-dimensional navier–stokes simulation,” *Journal of Fluid Mechanics*, vol. 365, pp. 23–88, Jun. 1998, ISSN: 1469-7645. DOI: 10.1017/S0022112098001116.
- [12] CANUTO, D. and TAIRA, K., “Two-dimensional compressible viscous flow around a circular cylinder,” *Journal of Fluid Mechanics*, vol. 785, pp. 349–371, 2015.

- 
- [13] DENNIS, S. and CHANG, G.-Z., "Numerical solutions for steady flow past a circular cylinder at reynolds numbers up to 100," *J. Fluid Mech*, vol. 42, no. 3, pp. 471–489, 1970.
- [14] FORNBERG, B., "A numerical study of steady viscous flow past a circular cylinder," *Journal of Fluid Mechanics*, vol. 98, no. 04, pp. 819–855, 1980.
- [15] LINNICK, M. N. and FASEL, H. F., "A high-order immersed interface method for simulating unsteady incompressible flows on irregular domains," *Journal of Computational Physics*, vol. 204, no. 1, pp. 157–192, 2005.
- [16] COUTANCEAU, M. and BOUARD, R., "Experimental determination of the main features of the viscous flow in the wake of a circular cylinder in uniform translation. part 1. steady flow," *Journal of Fluid Mechanics*, vol. 79, no. 02, pp. 231–256, 1977.
- [17] TRITTON, D., "Experiments on the flow past a circular cylinder at low reynolds numbers," *Journal of Fluid Mechanics*, vol. 6, no. 04, pp. 547–567, 1959.
- [18] BREHM, C., HADER, C., and FASEL, H. F., "A locally stabilized immersed boundary method for the compressible navier–stokes equations," *Journal of Computational Physics*, vol. 295, pp. 475–504, 2015.
- [19] GRESHO, P. M., CHAN, S. T., LEE, R. L., *et al.*, "A modified finite element method for solving the time-dependent, incompressible navier-stokes equations. part 1: Theory," *International Journal for Numerical Methods in Fluids*, vol. 4, no. 6, pp. 557–598, 1984.
- [20] SAIKI, E. and BIRINGEN, S., "Numerical simulation of a cylinder in uniform flow: Application of a virtual boundary method," *Journal of Computational Physics*, vol. 123, no. 2, pp. 450–465, 1996.
- [21] LIU, C., ZHENG, X., and SUNG, C., "Preconditioned multigrid methods for unsteady incompressible flows," *Journal of Computational Physics*, vol. 139, no. 1, pp. 35–57, 1998.
- [22] BERGER, E. and WILLE, R., "Periodic flow phenomena," *Annual Review of Fluid Mechanics*, vol. 4, no. 1, pp. 313–340, 1972.
- [23] CLIFT, R., GRACE, J. R., and WEBER, M. E., *Bubbles, drops, and particles*. Courier Corporation, 2005.
- [24] BELOV, A., MARTINELLI, L., and JAMESON, A., "A new implicit algorithm with multigrid for unsteady incompressible flow calculations," *AIAA paper*, vol. 95, p. 0049, 1995.
- [25] MIYAKE, T., SAKAMOTO, Y., TOKUNAGA, H., *et al.*, "Numerical solution of incompressible flow using two-step, one-stage runge-kutta time integration scheme," in *1st European Computational Fluid Dynamics Conference, Brussels, Belgium*, 1992, pp. 7–11.
- [26] BREHM, C., HADER, C., and FASEL, H. F., "A locally stabilized immersed boundary method for the compressible navier–stokes equations," *Journal of Computational Physics*, vol. 295, pp. 475–504, 2015.

- 
- [27] HARTMANN, R., “Numerical analysis of higher order discontinuous Galerkin finite element methods,” in *VKI LS 2008-08: CFD - ADIGMA course on very high order discretization methods*, Oct. 13-17, 2008, DECONINCK, H., Ed., Von Karman Institute for Fluid Dynamics, Rhode Saint Genèse, Belgium, 2008.

---



---

## List of Figures

3.1. Comparison of FEM, FVM and DG . . . . .	7
4.1. Cut cell with physical (red) and void region (white) [9] . . . . .	13
4.2. Cell agglomeration, taken from [9] . . . . .	15
5.1. Convergence Plot . . . . .	18
5.2. Isolines of pressure . . . . .	18
5.3. Convergence Plot . . . . .	20
5.4. Mesh size $128 \times 128$ , $P = 3$ . . . . .	20
6.1. Overview of Base Suction Coefficients over Reynolds Number [10] . . . . .	23
6.2. Recirculation Region [10] . . . . .	23
6.3. Kármán Vortex Street [10] . . . . .	24
6.4. Wake separation length, taken from [10], modified . . . . .	25
6.5. Graphical Presentation of Table 6.3 for $Re = 20$ . . . . .	27
6.6. Coefficient of Drag over Time ( $Re = 20$ ) . . . . .	28
6.7. Vorticity for DG3CpD60 for $Re = 20$ . . . . .	28
6.8. Graphical Presentation of Table 6.6 for $Re = 40$ . . . . .	30
6.9. Coefficient of Drag over Time ( $Re = 40$ ) . . . . .	30
6.10. Vorticity for DG3CpD60 for $Re = 40$ . . . . .	31
6.11. Lift coefficient over time for $0s < t < 150s$ ( $Re = 100$ ) . . . . .	34
6.12. Lift coefficient over time for $90s < t < 150s$ ( $Re = 100$ ) . . . . .	34
6.13. Drag coefficient over time for $90s < t < 150s$ ( $Re = 100$ ) . . . . .	34
6.14. Vorticity for DG3CpD60 for $Re = 100$ . . . . .	35
6.15. Lift coefficient over time for $0s < t < 150s$ ( $Re = 200$ ) . . . . .	38
6.16. Lift coefficient over time for $90s < t < 150s$ ( $Re = 200$ ) . . . . .	38
6.17. Drag coefficient over time for $90s < t < 150s$ ( $Re = 200$ ) . . . . .	38
6.18. Vorticity for DG3CpD60 for $Re = 200$ . . . . .	39
A.1. Mesh Used in the Robustness Study . . . . .	XIV
A.2. Mesh for CpD40 . . . . .	XIV
A.3. Mesh for CpD60 . . . . .	XV
A.4. Mesh for CpD80 . . . . .	XV

---

## List of Tables

3.1. Butcher Tableau for the Explicit Runge–Kutta Method. . . . .	11
3.2. Butcher Tableaus for different orders of RK . . . . .	11
6.1. Degrees of Freedom for Different Simulation Properties . . . . .	24
6.2. Comparison of Results for $W^*$ and $C_D$ , taken from [2], modified . . . . .	26
6.3. $C_D$ Values for each simulation . . . . .	26
6.4. Wake Separation Lengths for Each Simulation ( $Re = 20$ ) . . . . .	26
6.5. Comparison of Results for $W^*$ and $C_D$ , taken from [2], modified . . . . .	29
6.6. $C_D$ Values for each simulation . . . . .	29
6.7. Wake Separation Lengths for Each Simulation ( $Re = 40$ ) . . . . .	29
6.8. Comparison of Results for $St$ , $C_D$ and $C_L$ , taken from [2], modified . . . . .	32
6.9. $C_D$ Values for Each simulation . . . . .	33
6.10. $C_L$ Values for Each Simulation ( $Re = 100$ ) . . . . .	33
6.11. Strouhal Numbers for Each Simulation ( $Re = 100$ ) . . . . .	33
6.12. Comparison of Results for $St$ , $C_D$ and $C_L$ , taken from [2], modified . . . . .	36
6.13. $C_D$ Values for Each simulation . . . . .	37
6.14. $C_L$ Values for Each Simulation ( $Re = 200$ ) . . . . .	37
6.15. Strouhal Numbers for Each Simulation ( $Re = 200$ ) . . . . .	37

---

# A Appendix

---

## A.1 Mesh properties

---

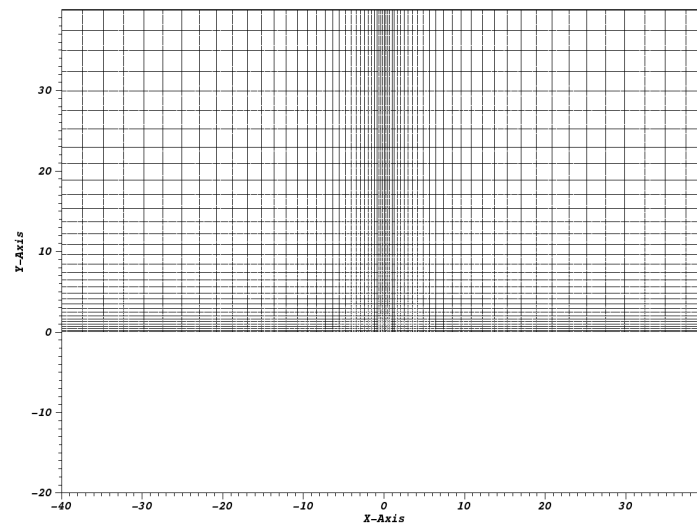


**Figure A.1.:** Mesh Used in the Robustness Study

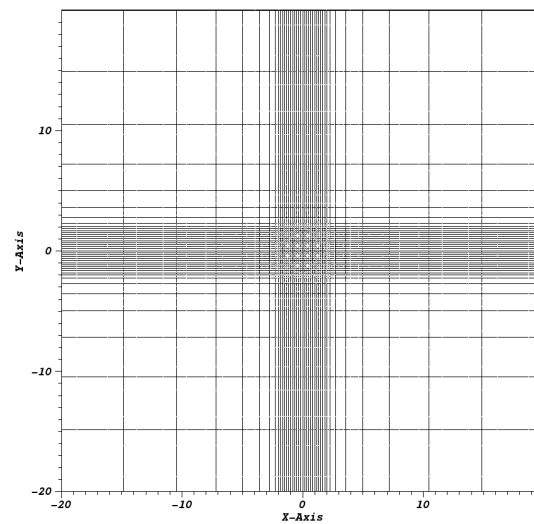


**Figure A.2.:** Mesh for CpD40

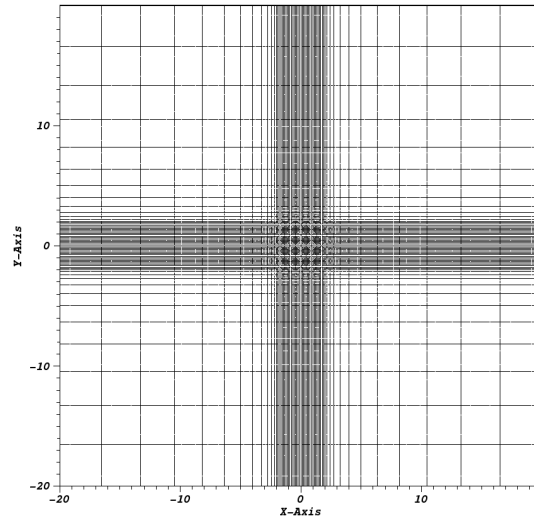


**Figure A.3.:** Mesh for CpD60

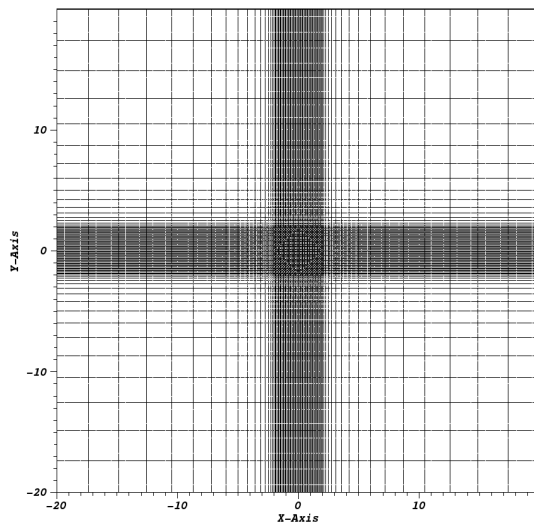


**Figure A.4.:** Mesh for CpD80